# Inverse Methods, Resolution and Implications for the Interpretation of Lithospheric Structure in Geophysical Inversions

Max Moorkamp[1], Javier Fullea[2], Richard Aster[3], and Bernhard Weise[4]

[1]Ludwig-Maximilians-Universitaet, Munich
[2]Instituto de Ciencias de la Tierra Jaume Almera,Dublin Institute of Advanced Studies Geophysics,Instituto de Geociencias
[3]Colorado State University
[4]University of Leicester

November 21, 2022

## Abstract

Inverse methods form the basis of many investigations of the structure of the lithosphere-asthenosphere system as they provide the basis for physics-based subsurface imaging from surface and/or near-surface measurements. Steady increases in computational capabilities and methodological improvements have resulted in increasingly detailed three-dimensional models of the Earth based on inverse methods. While these models can show an impressive array of features, it may be difficult for non-specialists to assess which aspects can be considered reliable and which are tenuous, or are artefacts of the mathematical formulation or data collection. In this paper we address the fundamental issues of feature reliability due to limited resolution and model sensitivity to data noise for researchers who do not work with intimately with inverse methods. We include and introductory overview of the mathematical formulation of inversion methods and define commonly used terms and concepts. We then present two case studies based on data from USArray in the western United States. The first case study utilizes magnetotelluric array data to construct a three-dimensional model of electrical resistivity to a depth of approximately 300 km. We use this example to demonstrate fundamental issues regarding data fit, data coverage, and model parameterization. The second case study discusses how we can incorporate petrological and mineral physics information directly into the inversion approach to create models that are compatible with constraints on the temperature and composition of the lithosphere. We will discuss the implications for practical use of these models in interpretations and provide guidelines on how to evaluate such models.

# Inverse Methods, Resolution and Implications for the Interpretation of Lithospheric Structure in Geophysical Inversions

Moorkamp, M.

*Ludwig Maximilians University, Munich, Germany*

Fullea, J.

*Complutense University of Madrid, Spain, and Dublin Institute for Advanced Studies, Ireland*

Aster, R.C.

*Geosciences Department, Warner College of Natural Resources, Colorado State University, Fort Collins, CO, USA*

Weise, B.

*University of Leicester, Leicester, UK*

## Abstract

Inverse methods form the basis of many investigations of the structure of the lithosphere-asthenosphere system as they provide the basis for physics-based subsurface imaging from surface and/or near-surface measurements. Steady increases in computational capabilities and methodological improvements have resulted in increasingly detailed three-dimensional models of the Earth based on inverse methods. While these models can show an impressive array of features, it may be difficult for non-specialists to assess which aspects can be considered reliable and which are tenuous, or are artefacts of the mathematical formulation or data collection. In this paper we address the

fundamental issues of feature reliability due to limited resolution and model sensitivity to data noise for researchers who do not work with intimately with inverse methods. We include and introductory overview of the mathematical formulation of inversion methods and define commonly used terms and concepts. We then present two case studies based on data from USArray in the western United States. The first case study utilizes magnetotelluric array data to construct a three-dimensional model of electrical resistivity to a depth of approximately 300 km. We use this example to demonstrate fundamental issues regarding data fit, data coverage, and model parameterization. The second case study discusses how we can incorporate petrological and mineral physics information directly into the inversion approach to create models that are compatible with constraints on the temperature and composition of the lithosphere. We will discuss the implications for practical use of these models in interpretations and provide guidelines on how to evaluate such models.

## 1. Introduction

The rigid lithosphere, and its transition to rheologically weak upper mantle across the lithosphere-asthenosphere boundary (LAB), are fundamental features of Earth's plate tectonic system, with the LAB constituting the principal detachment within the global plate tectonic system (e.g., Rychert and Shearer, 2009). The imaging and interpretation of processes and structures within the lithosphere and the asthenospheric mantle is advancing as geophysical data and methods along with complementary petrological and

mineral physics studies improve. However, lithospheric and LAB structures show complexity in both scale and detail, especially beneath the continents (e.g., Eaton et al., 2009), and differing methods of inversion and characterization, including thermal, seismic electrical, rheological and petrological techniques, may resolve different features within a lithosphere-asthenosphere transition zone between rigid to convecting mantle. In addition, inverse problems commonly exhibit mathematical ill-posedness and often have limited resolution, which result in high model sensitivity to data noise and in models that exhibit non-uniqueness and/or strong trade-offs between their parameters, respectively. Geophysical inversion is thus a powerful tool to image lithospheric structure and processes but its results must be tested and interpreted carefully in this context to avoid mis- and/or over-interpretation.

Here, we overview methodological and information issues of geophysical inversion in the context of studies of the lithosphere and asthenosphere. The text is addressed to an audience interested in applying geophysical inversion techniques but not necessarily familiar with the theoretical, practical, and interpretation problems inherent to the method. We first overview the mathematical description of inverse problems and solution approaches. Some of these concepts are also illustrated in the appendix through a highly simplistic Bouguer slab gravity problem that illustrates fundamental issues relevant to geophysical inversions. In the second part, we focus on practical aspects of geophysical inversion problems: finding the balance between model regularization and data fit, the effect of data coverage, and the influence of the model parameterization. To that aim we present an instructive example using magnetotelluric data from the EarthScope USArray project. In the third part we

deal with geophysical inversions focused on the primary (i.e., temperature, composition etc.) rather than the secondary (e.g., seismic velocities, electrical conductivity, density) physical parameters commonly used to describe the Earth. We illustrate the coupling between geophysical, petrological and mineral physics and the inherent issues and limitations attached to integrated inversions for the Earth's physical state in an study case where we invert surface wave, heat flow and elevation data for the lithospheric thermochemical structure in two columns representative of different tectonic terranes covered by the EarthScope USArray project.

## 2. Mathematical Characteristics of Inverse Problems

The generation and interpretation of physical models from data is a fundamental activity of geophysics. Ideally, we collect data that can constrain a unique model that is consistent with true Earth properties to arbitrary accuracy. Practical and theoretical issues, however, often prevent this. We summarize these issues and considerations in the context of the interpretation and characterization of lithosphere-scale Earth models for a broad community of geoscientists. Readers interested in more detailed development and discussion are invited to consult more specialized and extensive references on the subject (e.g., Tarantola, 1987; Baumeister, 1987; Menke, 1989; Kirsch, 1996). The following development utilizes the conventions and development in the text and appendices of Aster et al. (2018). Note in particular that vectors and matrices are denoted below as bold face lower-case and upper-case symbols, respectively.

Inverse problems, and the assessment and interpretation of their solutions,

can present multiple mathematical and philosophical challenges, even when underlying physical and mathematical models are effectively exact. Principal issues are conceptually depicted in Fig. 1.

## 2.1. The Forward and Inverse Problems

Conceptually, we may envision a "true" Earth model, which may be deterministic (i.e., we retrieve a single set of model parameters or coefficients), or statistical (i.e., the model is a probability density function). We wish to estimate the Earth model through the collection and inversion of relevant data. The relationships between data and model are characterized by the mathematical mapping between model and data parameters (the *forward problem*), reciprocally, between data and model parameters (the *inverse problem*) (Figure1). The forward and inverse problems are solved by mathematical and/or algorithmic procedures, which we generically denote as $g$ and $g^{-1}$, and which may be implemented using methods that range from closed-form mathematical expressions to complex iterative operations. The data are commonly time- and/or space-registered sets of numbers, ideally with reliable error estimates. The Earth model may be a corresponding set of time- and/or space-registered physical values, a probability density function, or parameters in a functional relationship. The forward problem of mapping models $m$ to data $d$ can be characterized as

$$g(m) = d \tag{1}$$

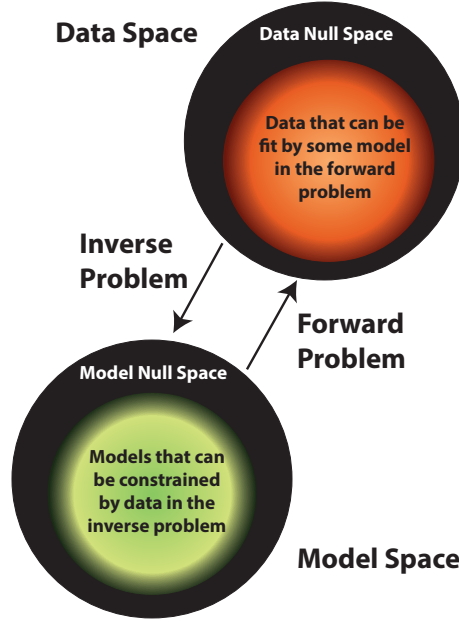and the inverse problem as

$$g^{-1}(d) = m \ . \tag{2}$$

Figure 1: Schematic relationship between the forward and inverse problems, and the model and data spaces. The forward problem and inverse problem are the mathematical and/or algorithmic procedures used to map between the two spaces. The data null space encompasses data projections that cannot be fit by any model (and this contribute only to the data misfit). The existence of a nontrivial (empty) data null space thus results in a nonzero data residual (14). The model null space encompasses models that cannot be constrained by any data via the inverse mathematical model, because they produce zero data predictions when inserted into the forward problem. The existence of a nontrivial model null space will result in imperfect model resolution.

## 2.2. Linearity and Nonlinearity

If a general mathematical operator $f$ is linear, then it satisfies superposition and scaling, such that

$$f(m_1 + m_2) = f(m_1) + f(m_2) \tag{3}$$

and

$$f(\alpha m) = \alpha f(m) \ . \tag{4}$$

Mathematical linearity in forward and inverse problems is associated with a rich body of insightful and practical mathematics and with very widely utilized solution methods (e.g., Menke, 1989). If $g$ is a linear forward problem operator, (3) implies that the data set predicted by a superposition model $\mathbf{m}_1 + \mathbf{m}_2$ is just the sum of the two respective data sets, $\mathbf{d}_1 + \mathbf{d}_2$, predicted by models $\mathbf{m}_1$ and $\mathbf{m}_2$. (4) implies that multiplying a model by a scalar $\alpha$ scales the predicted data by that same factor (and thus implies that the predicted data from the zero model is also zero). If a forward problem is linear, $\mathbf{d}$ and $\mathbf{m}$ are vectors describing the data and model, and $\mathbf{g}$ is a corresponding vector operation for the forward problem, then the forward problem can always be expressed in the form of a linear system of equations

$$\mathbf{g(m)} = \mathbf{Gm} = \mathbf{d} \tag{5}$$

where $\mathbf{G}$ is an appropriately sized matrix.

Geophysical inverse problems may be either linear (e.g., a basic gravity inversion for a density distribution), or nonlinear (e.g., seismic refracted-ray tomography or magnetotelluric inversion). Nonlinear problems are generally more complicated to approach because the powerful formalisms of lin-

7

ear algebra and integral and differential transformations do not directly apply. However, many nonlinear solution methods invoke iterative linearization strategies (e.g., Nocedal, 2006). Nonlinear problems may be additionally complicated by the presence of multiple locally optimal solutions.

*2.3. Rank Deficiency, Ill-Posedness, and Resolution*

Ideally, a noise-free data set $\mathbf{d}_{\text{true}}$ can be inverted to recover a unique model that is equal to the true Earth model, $\mathbf{m}_{\text{true}}$, so that

$$\mathbf{g}^{-1}(\mathbf{d}_{\text{true}}) = \mathbf{m}_{\text{true}} \ . \tag{6}$$

However, this ideal situation is non-realizable due to both theoretical and practical reasons.

First, some projection of $\mathbf{m}_{\text{true}}$, $\mathbf{m}_0$ may lie in the model null space (Fig. 1). Null space models by definition have no influence on the forward model-predicted data, so that

$$\mathbf{d}_{\text{true}} = \mathbf{g}(\mathbf{m}_{\text{true}}) = \mathbf{g}(\mathbf{m}_{\text{true}} + \mathbf{m}_0) \ . \tag{7}$$

and the data vector elements will thus contain no information that can constrain $\mathbf{m}_0$. If $\mathbf{g}$ is linear, (7) can always be written in matrix form ((5)) as

$$\mathbf{d}_{\text{true}} = \mathbf{G}(\mathbf{m}_{\text{true}} + \mathbf{m}_0) = \mathbf{G}\mathbf{m}_{\text{true}} + \mathbf{G}\mathbf{m}_0 = \mathbf{G}\mathbf{m}_{\text{true}} \tag{8}$$

where $\mathbf{G}$ is a matrix that implements the forward problem. The model null space in the linear case is thus the set of all models where

$$\mathbf{G}\mathbf{m}_0 = \mathbf{0} \tag{9}$$

8

which is the set of all model parameters whereby the columns of $\mathbf{G}$ can be linearly combined by the matrix-vector product (9), with the coefficients being the elements of $\mathbf{m}_0$, to produce the zero vector. If such a linear combination is possible for nonzero coefficients (i.e., $\mathbf{m}_0 \neq \mathbf{0}$), then $\mathbf{G}$ is *rank deficient*. Rank deficiency commonly arises in inverse problems (e.g., tomography) because some combinations of the model parameters (e.g., adjacent seismic velocity cells or nodes in a tomography problem) are not uniquely determined by the available data. An instructive visual example of null-space models for magnetic data is shown in Maus and Haak (2003).

Another important situation that commonly arises in inverse problems is where the solution is highly sensitive to small changes in the data. Consider a linear problem expressed as a model vector $\mathbf{m}$ and a forward problem matrix $\mathbf{G}$. We seek a solution $\mathbf{m}$ that fits the data by satisfying (5). To achieve this, we seek an appropriate inverse matrix that recovers $\mathbf{m}$ given $\mathbf{d}$. If $\mathbf{G}$ is a square matrix and is not rank deficient (or equivalently, is nonsingular), it will have a unique inverse $\mathbf{G}^{-1}$ and the inverse problem is straightforwardly solved as

$$\mathbf{m} = \mathbf{G}^{-1}\mathbf{d} \tag{10}$$

where $\mathbf{G}^{-1}$ is the standard inverse of a square matrix where

$$\mathbf{G}^{-1}\mathbf{G} = \mathbf{G}\mathbf{G}^{-1} = \mathbf{I} \tag{11}$$

and $\mathbf{I}$ is an identity matrix.

If $\mathbf{G}$ is not square, a *pseudo- or generalized inverse* can be constructed to solve the inverse problem. A widely implemented generalized inverse is the

*Moore-Penrose pseudoinverse*, $\mathbf{G}^\dagger$, which produces a solution

$$\mathbf{m}_\dagger = \mathbf{G}^\dagger \mathbf{d} \ . \tag{12}$$

The solution given by (12) is of considerable practical interest in that it has two often desirable least-squares properties. First, the solution is minimum-length, in the sense that the 2–norm of the model

$$\|\mathbf{m}_\dagger\|_2 = \sqrt{m_{\dagger,1}^2 + m_{\dagger,2}^2 + \ldots + m_{\dagger,n}^2} \ . \tag{13}$$

will be minimized. Second, the pseudoinverse solution will have a minimum data misfit in the sense that the 2–norm of the *residual vector* characterizing the 2–norm distance between observed and model-predicted data

$$\|\mathbf{r}\|_2 = \|\mathbf{d} - \mathbf{G}\mathbf{m}_\dagger\|_2 \tag{14}$$

is minimized. These two properties result in $\mathbf{m}_\dagger$ having no projection in the model null space, since any such projection would increase (13) without changing (14).

The normalized degree to which small changes (e.g., errors caused by noise or round-off) in the elements of $\mathbf{d}$ may affect the model obtained in (10) or (12) is bounded by the *condition number*, $c$, of $\mathbf{G}$. This relationship is characterized for a general norm by

$$\frac{\|\mathbf{m} - \hat{\mathbf{m}}\|}{\|\mathbf{m}\|} \leq c \, \frac{\|\mathbf{d} - \hat{\mathbf{d}}\|}{\|\mathbf{d}\|} \tag{15}$$

where $\mathbf{d}$ is noise-free data, $\hat{\mathbf{d}}$ is perturbed (e.g., noisy) data, $\mathbf{m}$ is the model recovered from $\mathbf{d}$ and $\hat{\mathbf{m}}$ is the perturbed model recovered from $\hat{\mathbf{d}}$. For the 2–norm and Moore-Penrose generalized inverse solution, the condition number is given by

$$c = \text{cond}(\mathbf{G}) = \|\mathbf{G}\|_2 \|\mathbf{G}^\dagger\|_2 = \sqrt{\lambda_{\max}/\lambda_{\min}} \tag{16}$$

10

where the $\lambda$ are the maximum and minimum (real-valued) eigenvalues of the (square and symmetric) matrix $\mathbf{G}^T\mathbf{G}$. A system of equations with a large condition number is referred to as *ill-posed*. In an ill-posed inverse problem, exact (or nearly so), data fitting, even if mathematically possible, is ill-advised. This is because, practically speaking, data will always have some level of inaccuracy. Fortunately, useful solutions to such problems can be found by fitting the data to an appropriate tolerance, as dictated by the data uncertainty, often while imposing additional stabilizing and/or physical constraints on the model as described below.

Geophysical inverse problems are commonly ill-posed because the physics of the associated forward problems are characterized by integral equations (or in their discretized versions, by approximating Riemann sums) in which rapid or sharp (in time or space) model variations become highly smoothed in their influence on predicted data (e.g., Avdeev, 2005). The corresponding inverse solution will thus conversely exhibit high sensitivity to data noise or other data perturbations. In linear problems, discretizing such systems into systems of linear equations (5) can produce $\mathbf{G}$ matrices with extremely large condition numbers. In the case of a rank deficient $\mathbf{G}$, the condition number will be effectively infinite, since $\lambda_{\min}$, and perhaps other eigenvalues of $\mathbf{G}^T\mathbf{G}$ in (16), will be zero.

Rank deficiency and ill-posedness present formidable challenges to inverse problems. However, if data acquisition and model parameterization are well designed, their effects can be minimized so that valuable models may still be recovered in such problems. One key approach to eliminate rank deficiency and reduce ill-posedness is to impose additional, stabilizing, constraints via

*regularization* (e.g., Farquharson and Oldenburg, 1998; Aster et al., 2018). A conceptually analogous process, the use of probabilistic model priors, is utilized in Bayesian inversion (described below).

## 2.4. Classical and Bayesian Approaches

The above theoretical development for inverse problems, which commonly incorporates a data set with an associated statistical uncertainty, a deterministic forward and inverse problem, and in which a "preferred" model (or set of models) is solved for subject to constraints, may be referred to as a *classical* perspective (e.g., Tarantola, 1987; Aster et al., 2018). In this viewpoint, the recovered model $\mathbf{m}$ is an estimate of Earth properties that we seek, through experiment design, data collection, and an inverse methodology. Such models are described by functions or by discrete parameters.

In the Bayesian philosophy, the model is a probability density function constrained via the mathematics of the forward problem and is conditioned to be statistically optimal with respect *a priori model constraints* or model *priors*. Bayesian models are commonly estimated using computationally intensive (e.g., Markov Chaim Monte Carlo) sampling methods and have become extensively utilized in geophysics as computational and data resources have expanded (e.g., Malinverno and Briggs, 2004; Tarantola, 2005; Roy and Romanowicz, 2017).

Bayes' Theorem

$$q(\mathbf{m}|\mathbf{d}) = \frac{f(\mathbf{d}|\mathbf{m})p(\mathbf{m})}{c} \tag{17}$$

is the fundamental equation of Bayesian inference and Bayesian inverse the-

ory, where the constant

$$c = \int_{\text{all models}} f(\mathbf{d}|\mathbf{m})p(\mathbf{m}) \, d\mathbf{m} \; . \tag{18}$$

$q(\mathbf{m}|\mathbf{d})$, the *posterior distribution*, is the probability of a model $\mathbf{m}$, given a data set $\mathbf{d}$, $p(\mathbf{m})$ is an assigned prior distribution that provides added statistical constraints to the solution, and $f(\mathbf{d}|\mathbf{m})$ is a *likelihood function* that calculates the probability of observing the data $\mathbf{d}$ given a model $\mathbf{m}$. In practice, $f(\mathbf{d}|\mathbf{m})$ is commonly repeatedly calculated for a range of trial models using the mathematics of the forward problem to successively sample the desired posterior probability $q$ for a given data set. If the dimension of the model space $\mathbf{m}$ is large, this sampling must be done cleverly (e.g., using Metropolis-Hastings Markov Chain Monte Carlo or other such methods) to efficiently sample $q$, or the sampling process may become intractable for even very fast computers. $c$ is a normalizing factor to scale the posterior so that it is a proper probability density function (i.e., so that it integrates to one over all models), but calculating its value is often noncritical. A remarkable and valuable aspect of (17) is that it accommodates linear and nonlinear likelihood functions with equal facility.

Once a posterior distribution is estimated it can be interrogated to retrieve probabilistic statements about the model (e.g., what is the probability that values within a particular region of a seismic velocity structure lies is within a specified range or region (e.g., the lithopshere or asthenosphere). Sometimes, the specific model that maximizes $q(\mathbf{m}|\mathbf{d})$; referred to as the *maximum a posteriori* or *MAP* model) is also reported, although appropriate accompanying probabilistic information about the posterior distribution is required to put it into context.

A point of mathematical unification between the classical and Bayesian approaches (which will be utilized in the inversion discussed in Section 4) occurs for the least-squares solution that minimizes an *objective function* of the form

$$[\mathbf{Gm} - \mathbf{d}]^T \mathbf{C}_D^{-1} [\mathbf{Gm} - \mathbf{d}] + [\mathbf{m} - \mathbf{m}_{\text{ref}}]^T \mathbf{C}_M^{-1} [\mathbf{m} - \mathbf{m}_{\text{ref}}]) \qquad (19)$$

(e.g., Tarantola, 2005; Aster et al., 2018). Here, $\mathbf{m}_{\text{ref}}$ is a reference model (or prior, in the corresponding Bayesian problem) with covariance matrix $\mathbf{C}_M$ and $\mathbf{C}_D$ is the data covariance matrix. The first term specifies that the data be fit in the sense that the 2–norm of $\mathbf{C}_D^{-1/2}(\mathbf{Gm} - \mathbf{d})$ will be small. The second term introduces regularization by specifying that the solution $\mathbf{m}$ be close to $\mathbf{m}_{\text{ref}}$ in the sense that the 2–norm of $\mathbf{C}_M^{-1/2}(\mathbf{m} - \mathbf{m}_{\text{ref}})$ will be small, where the $-1/2$ exponents indicate the matrix square roots of the inverse covariance matrices in (19). The balance between data fit versus adherence to the regularization condition is controlled by the inverses of the covariance weighting matrices $\mathbf{C}_D$ and $\mathbf{C}_M$. The least-squares minimizing solution to the classical minimization problem 19 is identical to the MAP solution for the corresponding Bayesian problem there the prior distribution $\mathbf{m}_{\text{ref}}$ has an multivariate (MVN) distribution specified by its mean value and $\mathbf{C}_M$, the data elements are MVN distributed as described by their values and $\mathbf{C}_D$. The solution may be found by solving the least-squares problem

$$\begin{bmatrix} \mathbf{C}_D^{-1/2} \mathbf{G} \\ \mathbf{C}_M^{-1/2} \end{bmatrix} \mathbf{m} = \begin{bmatrix} \mathbf{C}_D^{-1/2} \mathbf{d} \\ \mathbf{C}_M^{-1/2} \mathbf{m}_{\text{ref}} \end{bmatrix} . \qquad (20)$$

and will have a covariance matrix given by

$$\tilde{\mathbf{C}}_M = \left( \mathbf{G}^T \mathbf{C}_D^{-1} \mathbf{G} + \mathbf{C}_M^{-1} \right)^{-1} . \qquad (21)$$

14

*2.5. Model Uncertainty and Resolution*

Both the classical and Bayesian methodologies would at first appear to offer straightforward ways to estimate model uncertainty. In the classical case, one may propagate a data covariance matrix or a Monte-Carlo set of random data realizations through the solution methodology to produce confidence interval and model parameter correlations (the *formal or stochastic uncertainty*). In the Bayesian case, probabilistic bounds on model features may be calculated as marginal probabilities of the posterior distribution. However, for ill-posed or rank deficient problems a larger epistemological issue commonly arises because of solution nonuniqueness, ill-posedness.

In the classical methodology, nonuniqueness and ill-posedness are addressed by imposing regularization. The mathematical form of the resulting solution bias is typically chosen to limit the range of "good" models to those with (hopefully) realistic properties. Many regularization approaches have been explored and applied for such problems, and multiple approaches may be implemented simultaneously. Example regularization strategies include penalizing a solution size metric (e.g., defined by the 2–norm (13), or other sense), its smoothness, minimizing excursion from some reference model (e.g., (19)), minimizing the number of allowed discontinuities and their magnitudes, imposing model sparsity, specifying non-negativity or other restrictions to parameter bounds, or implementing a more coarsely parameterized model with fewer but better resolved model parameters, a process referred to as *regularization by discretization*. However, the solution bias induced by regularization is difficult to usefully quantify because the true Earth model is of course unknown and any true model projections in the model null space

15

cannot be constrained by data. In insightful synthetic examples (where the "true" model is specified) regularization bias can commonly be shown to be much larger than the stochastic uncertainty.

The effects of regularization bias may be usefully assessed by calculating and interpreting the *model resolution*. For a general discretized linear problem, if we suppose the true model were $\mathbf{m}_{\text{true}}$, and the associated predicted data set were $\mathbf{d}_{\text{true}}$, then the associated forward problem (5) will be the linear system of equations

$$\mathbf{d}_{\text{true}} = \mathbf{G}\mathbf{m}_{\text{true}} \ . \tag{22}$$

Solving the inverse problem for this data set by applying a suitable inverse operator, such as the Moore-Penrose pseudoinverse, $\mathbf{G}^{\dagger}$, gives

$$\mathbf{m}_{\dagger} = \mathbf{G}^{\dagger}\mathbf{d}_{\text{true}} = \mathbf{G}^{\dagger}\mathbf{G}\mathbf{m}_{\text{true}} = \mathbf{R}\mathbf{m}_{\text{true}} \ . \tag{23}$$

However, in a rank deficient and/or regularized problem the *resolution matrix* $\mathbf{R}$ will not be an identity matrix, and $\mathbf{m}_{\dagger}$ will thus not generally be equal to $\mathbf{m}_{\text{true}}$, even for the "perfect" noise-free data of (22). The resolution matrix, and (23) thus describes the linear mapping of $\mathbf{m}_{\text{true}}$ to $\mathbf{m}_{\dagger}$ for a linear inverse problem. For any hypothetical Earth model, $\mathbf{m}_{\text{test}}$, we can thus characterize and assess its noise-free recovery via inversion as

$$\mathbf{m}_{\text{recov}} = \mathbf{R}\mathbf{m}_{\text{test}} \ . \tag{24}$$

In addition the recovery of the $i^{th}$ model parameter can be evaluated by considering an impulsive $\mathbf{m}_{\text{test}}$ in (24) that consists of all zeros, save a value of one in the $i^{th}$ element (or equivalently, by examining the $i^{th}$ column of $\mathbf{R}$). Resolution of the $i^{th}$ model parameter is considered "perfect" if the elements

of the corresponding resolution matrix column are zeros except for a value of one in the $i^{th}$ element. However, in limited resolution inversions the recovery of impulse test models will result in nonzero elements of the model vector that span multiple parameters, as we will see in the case study for North America below.

In a nonlinear problem, no such mathematically compact representation of resolution as (23) exists, but the mapping of a test model to a corresponding recovered model $\mathbf{m}_{\text{recov}}$ can be similarly calculated as the operation

$$\mathbf{m}_{\text{recov}} = \mathbf{g}^{-1}\left(\mathbf{g}(\mathbf{m}_{\text{test}})\right) \tag{25}$$

where $\mathbf{g}$ and $\mathbf{g}^{-1}$ represent vector-valued forward and inverse operators, respectively. For very large nonlinear problems, such as full seismic waveform adjoint tomography (e.g., Bozdağ et al., 2016; Lloyd et al., 2019), the computational cost of implementing (25) may be very high, and direct resolution tests of this type may not be practical, although some usable approximations exist (Fichtner and Trampert, 2011). Similar resolution exercises using test models and inversions of synthetic data can be performed in a Bayesian context.

Resolution is typically demonstrated and evaluated in published results using one or more resolution tests. One approach is to show the recovery of a test or idealized Earth model using (23 or 25). This may be done for a single perturbed parameter or a region of parameters (e.g., a representative subsurface feature), calculating synthetic data from this test model, sometimes adding data noise (although a formal calculation of $\mathbf{R}$ should be performed without data noise), and finally recovering a model using the preferred solution method. The recovery of a test model can provide valuable confirmatory

insight into critical aspects of feature localization (e.g., the resolvability of a seismic low velocity zone), amplitude, and other key metrics of a model. A commonly implemented special case of resolution testing is to use an alternating (e.g., "checkerboard") test model (e.g., Fishwick, 2010). For suitably small linear problems, if $\mathbf{R}$ is known, this process can be performed using (24), but for problems with very high dimensional model spaces the full calculation of the resolution matrix may be infeasible. However, instructive diagonal elements of $\mathbf{R}$ can be estimated stochastically in such situations (MacCarthy et al., 2011).

To Illustrate the concepts of this section with a simple example, we have included a demonstration example of a very simple gravity inverse problem in the Appendix to this paper.

## 3. Imaging and Interpretation of the Lithosphere-Asthenosphere System Using Inverse Modeling

The ultimate value of an inverse model depends on three critical issues. First is the method of solution and implications of model resolution and/or stochastic uncertainty. In essence, this issue reflects how closely the recovered model may represent the unknown true model. Second, is the (frequent) post-inversion interpretation or formal mapping of the model with respect to other physical quantities of interest, which often differ from the model units. Examples are the mapping of seismic velocity or electrical conductivity to temperature, composition, and or phase state. This second issue may require a relatively straightforward mapping or may be approached as a subsequent inverse problem, in which case it often includes the characteristic challenges

18

of ill-posedness and/or non-uniqueness. Third is the model interpretation in terms of relevant structure, history, and/or processes, which is commonly approached in the context of hypothesis testing.

## 3.1. Case Study: Magnetotelluric Inversion of USArray Data in the Western U.S.

To illustrate the issues above for imaging at the lithospheric scale, we focus on the western United States where the large-scale EarthScope USArray initiative has provided a unprecedented density of uniform and high-quality geophysical observations (e.g., Trabant et al., 2012; Kelbert, 2019). In particular seismological and magnetotelluric (MT) measurements have been collected on an unparalleled scale and sparked new insights into lithospheric structure in this region and more broadly (Long et al., 2014). Similar large geophysical array initiatives have more recently been launched in Australia, China and, to a lesser extent, in Europe (e.g., Robertson et al., 2016; Li et al., 2018; Hetényi et al., 2018). This example illuminates the difficulties in assessing the appropriate level of fit and finding an inversion model that represents the true Earth reliably.

For our initial demonstration we will focus on the MT inversion. MT is a passive electromagnetic technique that utilizes the natural time variations of naturally occurring electromagnetic fields at the surface recover subsurface resistivity (e.g., Chave and Jones, 2012). Studies that utilize the USArray MT data include (Patro and Egbert, 2008; Zhdanov et al., 2011; Kelbert et al., 2012; Meqbel et al., 2014; Bedrosian and Feucht, 2014). While these studies generally agree on many of the first–order features, they also show differences (particularly related to the deeper features, where resolution be-
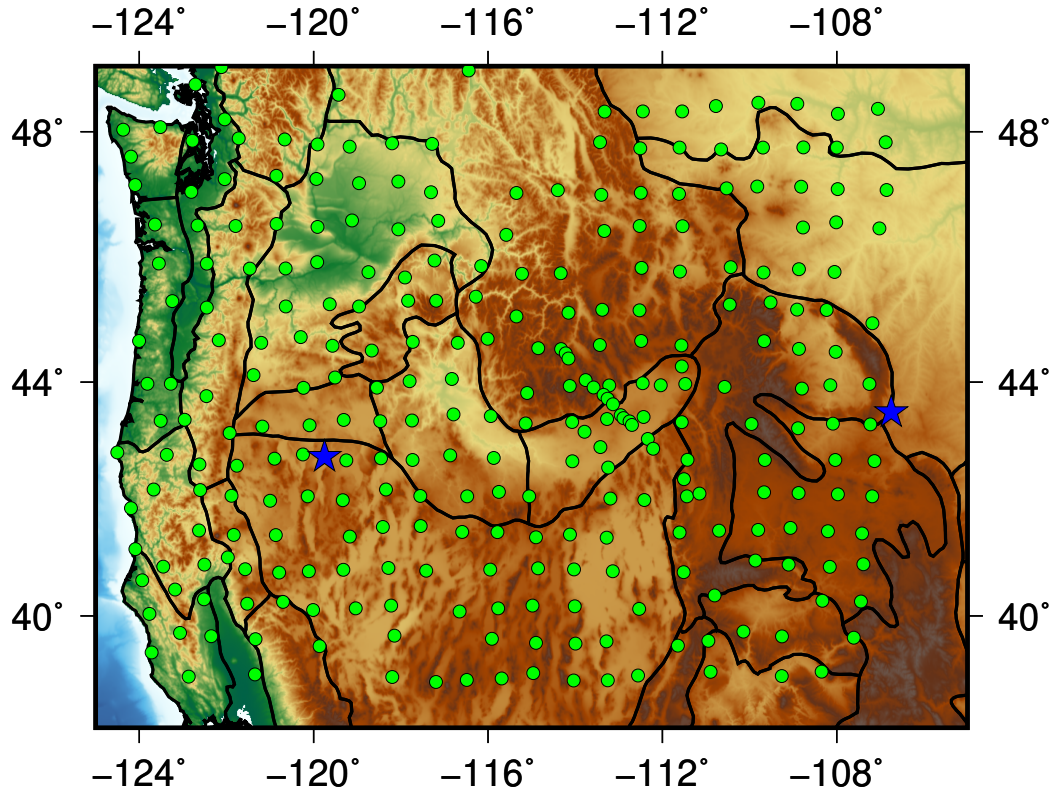
19

Figure 2: Topographic map of the northwestern United States. Locations of EarthScope USArray magnetotelluric (MT) stations used in the MT inversion case study in Section 3 are shown as green circles. Blue stars mark sites evaluated in the northern Basin and Range (W) and Wyoming Craton (E) provinces in the integrated petrophysical-geophysical modelling case study of Section 4 (Table 1). Black borders indicate physiographic unit boundaries.

comes more challenging) that reflect different inversion methodology choices.

One of the first questions when inverting geophysical data in practice is how well we should seek to fit the observations with our models, given that measurements will unavoidably contain systematic or random errors that may be difficult to estimate. Data misfit can be usefully summarized by the root-mean-square (RMS) value, given by the 2–norm of the weighted residual vector normalized by the number of data points (14)

$$\Phi = \sqrt{\frac{1}{m} \sum_{i=1}^{m} \left( \frac{d_i - \mathbf{G}(\mathbf{m})_i}{\sigma_i} \right)^2} = \sqrt{\frac{1}{m}} \|\mathbf{r}_w\|. \tag{26}$$

Here, $d_i$ is the $i^{th}$ data point, $m$ is the number of data points, the $\mathbf{G}(\mathbf{m})_i$ are the corresponding predicted data produced by the forward problem using a model of interest $\mathbf{m}$, the $\sigma_i$ are uncertainties (usually standard deviations) associated with each observation, and $\|\mathbf{r}_w\|$ is the 2–norm of $1/\sigma_i$ weighted residual terms, as modified from (14).

If the $\sigma_i$ are standard deviations characterizing normally distributed and independent data errors, then $\|\mathbf{r}_w\|^2$ is distributed as the chi-square distribution with $m-n$ degrees of freedom, where $n$ is the number of model parameters. For $m >> n$, the expected value of $\|\mathbf{r}_w\|^2$ is $m$, and the expected value of $\Phi$ under these conditions is one. More generally, the *discrepancy principle* (e.g., Aster et al., 2018) specifies that a heuristic data fit target in regularized problems where $n > m$ is to also seek solutions where $\Phi \approx 1$. Values much smaller than unity indicate that the average residual term is below the estimated noise level, i.e., we match the data better than the uncertainty. For ill-posed problems this is especially inadvisable because the over-fitting of noisy data will typically result in very large amplitude, wildly oscillating,

21

or otherwise unrealistic models. Conversely, $\Phi$ values much larger than one indicate that the mismatch between observations and predicted data is much larger than the estimated noise and the model does not sufficiently reproduce the observations. This can occur due to approximate or improper mathematical forward modeling, underestimation of data errors, and/or high degrees of regularization. While this strategy provides a simple criterion to judge the result and a strategy for choosing regularization parameters, in practice it may be difficult to apply rigorously (e.g., Miensopust, 2017; Aster et al., 2018), again because data uncertainties $\sigma_i$ are often difficult to estimate. For example, when inverting Bouguer-corrected gravity data, we can estimate uncorrelated instrument noise well, but it is difficult to assess the effect of terrain inaccuracies in the Bouguer correction. Similarly, in MT inversion, rigorous statistical methods are employed to estimate uncertainty bounds on the data (Chave, 2017). However, the presence of artificial electromagnetic sources (e.g., electrified livestock fences or other artificial interference), may produce erroneous data with inappropriately small uncertainty estimates (e.g., Rao et al., 2014).

Because of these difficulties, we may not be able to achieve an RMS value near unity for any model or may choose in favor of a more highly regularized and conservative model. Such a model will not reproduce the data as well but may also is more likely to contain unwarranted structure.

Figure 3 shows the comparison between data (symbols) and synthetic data (curves) produced by the forward problem for models with different RMS levels $\Phi$. As is common practice in MT imaging, we plot apparent resistivity ($\rho_a$) and phase ($\varphi$) of the four impedance elements as a function of
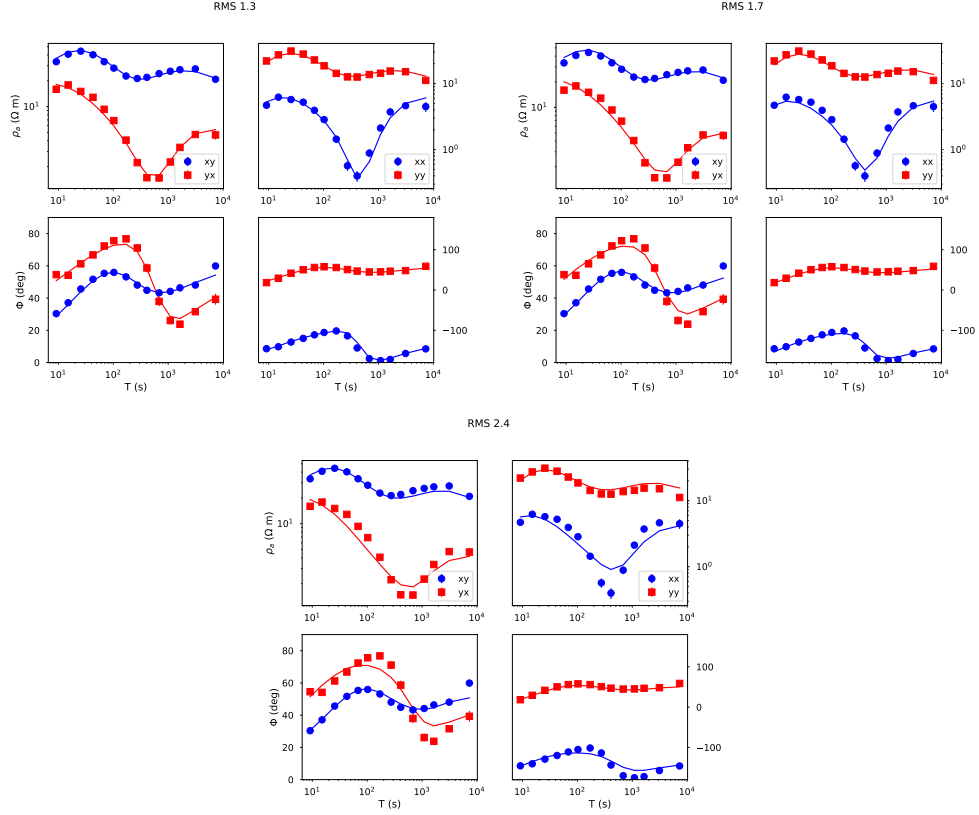
Figure 3: Comparison between data (symbols) and synthetic predictions (lines) for three different levels of RMS data misfit: $\Phi = 1.3$ (upper left), $\Phi = 1.7$ (upper right), $\Phi = 2.4$ (lower panels).

period ($T$). Although the data are plotted with error bars, at most periods the length of the formal error bars is smaller than the size of the data symbols. Furthermore, observed apparent resistivity and phase vary smoothly as a function of period, which is also suggestive of the high quality of the measurements. The recovered model for $\Phi = 1.3$ reproduces the observations at this site nearly perfectly, with only a few data points deviating visibly from the synthetic data predicted by the model. The highest deviations occur at the smallest and largest periods, which are influenced by the most shallow and deepest structures in the model, respectively. Such issues can occur due to paramterization issues, such as when the model cell size is not small enough (for the short periods) or the model does not extend deep enough (for the long periods). In this case these points appear to be downward shifted compared with the trend indicated by the rest of the measurements and thus the most likely explanation is a systematic shift caused by mild data noise that was not fully accounted for in the formal error estimate.

Imposing additional regularization to produce a data misfit increase to $\Phi = 1.7$, we start to see some model deviations. Particularly where the data change rapidly as a function of frequency, e.g., the $xy$-component apparent resistivity at periods between 500-1,000 s, the changes in the synthetic data are less pronounced. This becomes even more evident when regularization is further increased so that $\Phi$ increases to 2.4 (bottom plot in Figure 3). In this case, we observe that the synthetic data follow the general shape of the observations but does not reproduce the finer-scale details.

This kind of behavior is typical for regularized inversions in general and not a particular property of MT data. Rapid changes of data as a function
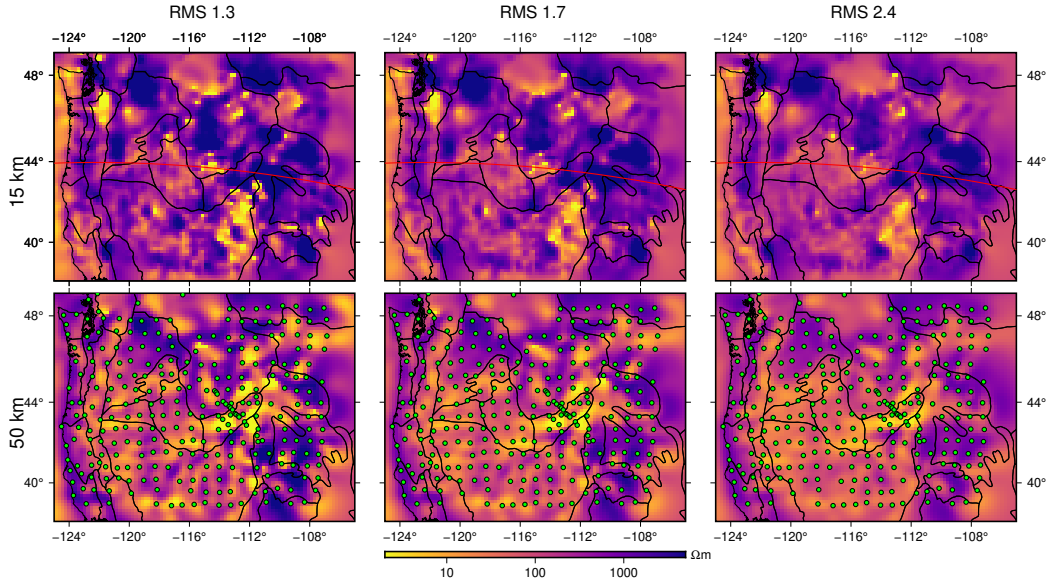
Figure 4: Horizontal slices through MT inversion models for different levels of misfit and regularization at a depth of 15 km (top row) and 50 km (bottom row). The red line shows the location of profiles in Figure 5.

of period, time or space are typically caused by abrupt changes in model properties. Regularization reduces the ill-posedness of the inverse problem, as explained above, by restricting the spatial variability of the model parameters (smoothness regularization corresponding to minimizing first differences between adjacent model values is used in this demonstration), or the deviation from a prior model (e.g., Egbert and Kelbert, 2012). This prevents the appearance of spurious structures due to noisy data, but also limits the ability of the inversion to fit the observations. Thus, it is necessary to balance the data fit with the degree of model structure and judging which trade-off between level of fit and parameter variability is realistic, commonly by exploring a suite of models that correspond to differing levels of regularization.

*3.1.1. The Trade-off Between Data Fit and Resolution*

Figure 4 shows two horizontal slices through the three resistivity models with different values of $\Phi$, and Figure 5 shows vertical E-W slices along the red profiles in Figure 4. The basic appearance of all these models is very similar. This reflects the stabilizing effect of the regularization, in this case, an imposition of smoothness. Close inspection does reveal some differences, however. As expected from the preceding discussion, the model with the lowest $\Phi$ value and least regularization displays the strongest resistivity contrasts, particularly at the shallowest depths. Moreover, we find a few small low resistivity features at 15 km depth that are only visible in the model with lowest value of $\Phi$ and any of these features are only associated with individual measurement sites in that the anomalies only occur in the model cell directly below a station site. This is an indication that with $\Phi = 1.3$ we are starting to allow structures that are not necessarily well constrained, i.e., we also fit aspects of the data that are due to noise. At $\Phi = 1.7$ this effect is reduced so that most structures extend over larger areas. This trend continues when $\Phi$ increases further to 2.4 and the model correspondingly becomes smoother. The long-wavelength resistivity image remains similar, but we start to lose details and the absolute contrasts are further reduced.

Based on trade-off between data fit and model smoothness (imposed by the level of regularizatoin), a $\Phi$ value between 1.3 and 1.7 is inferred to be optimal for this inversion. Within this range of misfit, the data fit is broadly within in the expected range based on data uncertainty estimates, the change of models is small, and interpretations will be consistent.

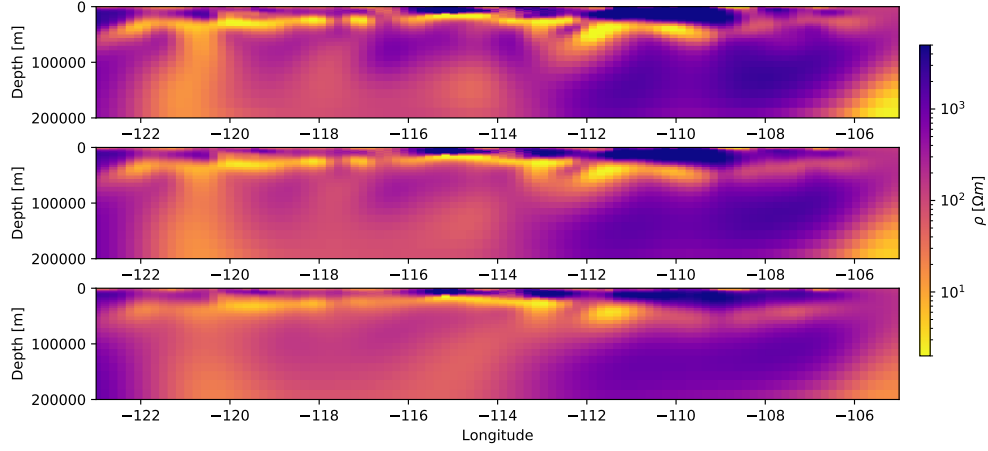A more detailed examination of data misfit above and beyond the $\Phi$ misfit

26

Figure 5: Vertical slices along the red line in Figure 4 for different levels of RMS $\Phi$. From top to bottom $\Phi = 1.3, \Phi = 1.7, \Phi = 2.4$.

measure can also be insightful when assessing a regularized inversion. A map view of misfits (Figure 6) for this problem shows that, for $\Phi = 1.3$, at most stations the misfit for all four components of impedance is comparable to the average misfit, i.e., most sites show a misfit between 1.0 and 2.0. There are a few isolated sites where the misfit exceeds 5.0 in a single component. However, these are surrounded by sites that are well fit. This suggests that the high misfit is caused by erroneous data with small error estimates or highly localized structures. When the overall data fit increases, we see that not only the average misfit at most sites increases, but also the variability of the misfit. This is particularly apparent when looking at the maps for $\Phi = 2.4$ in Figure 6. While many sites still show a misfit comparable with the average, now a significant number of sites exhibits outlier misfit values
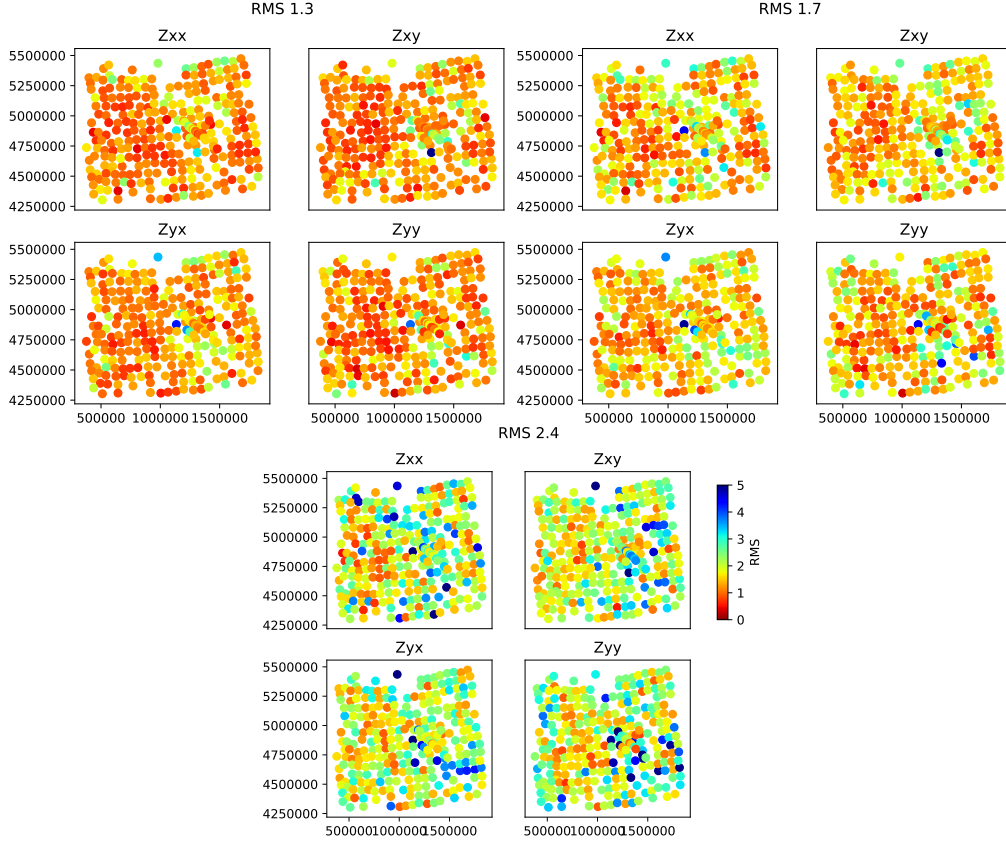
Figure 6: Maps of data misfit terms in (26) displayed at individual station sites. The overall misfit levels are $\Phi = 1.3$ (top left), $\Phi = 1.7$ (top right) and $\Phi = 2.4$ (bottom).

(e.g., larger than 5). Furthermore, we observe clusters of sites that show spatially correlated high misfits. This further suggests that there are larger-scale features of the true resistivity structure that are inadequately reflected in the model. This impression is also confirmed by the plots of misfit as a function of period and site number in Figure 7.

At the two smaller $\Phi$ value models, data with high misfit typically occurs in spatial isolation and neighbouring data show low misfit values. In contrast, for the highest ($\Phi = 2.4$) misfit model, we observe broad regions of misfit both along the period axis and the stations axis, i.e., we note several sites that have significant misfit across all periods and certain period bands are not well fit for many sites. Clustering of data points with high misfit in the spatial and period domains is an indicator of model over-regularization. In such cases, it is still necessary to closely inspect the data for possible systematic error issues. For example, in MT the period band between 1-10 s, the so-called dead band, tends to be noisier then other periods due to low signal levels (e.g., Chave and Jones, 2012) and disturbances from artificial noise sources can affect clusters of measurement points even over relatively large distances (e.g., Evans et al., 2011) and lead to regionally spurious data. While plots of misfit for each measurement sites as shown in Figure 6 can be utilized for most geophysical methods, the more detailed view provided by Figure 7 is method specific. For seismic tomography a suitable alternative is to plot travel-time or phase discrepancies for each ray-path (e.g., Fichtner et al., 2009), for example. In any case, a comprehensive look at the discrepancy between observations and model predictions is necessary to assess the quality of the model.
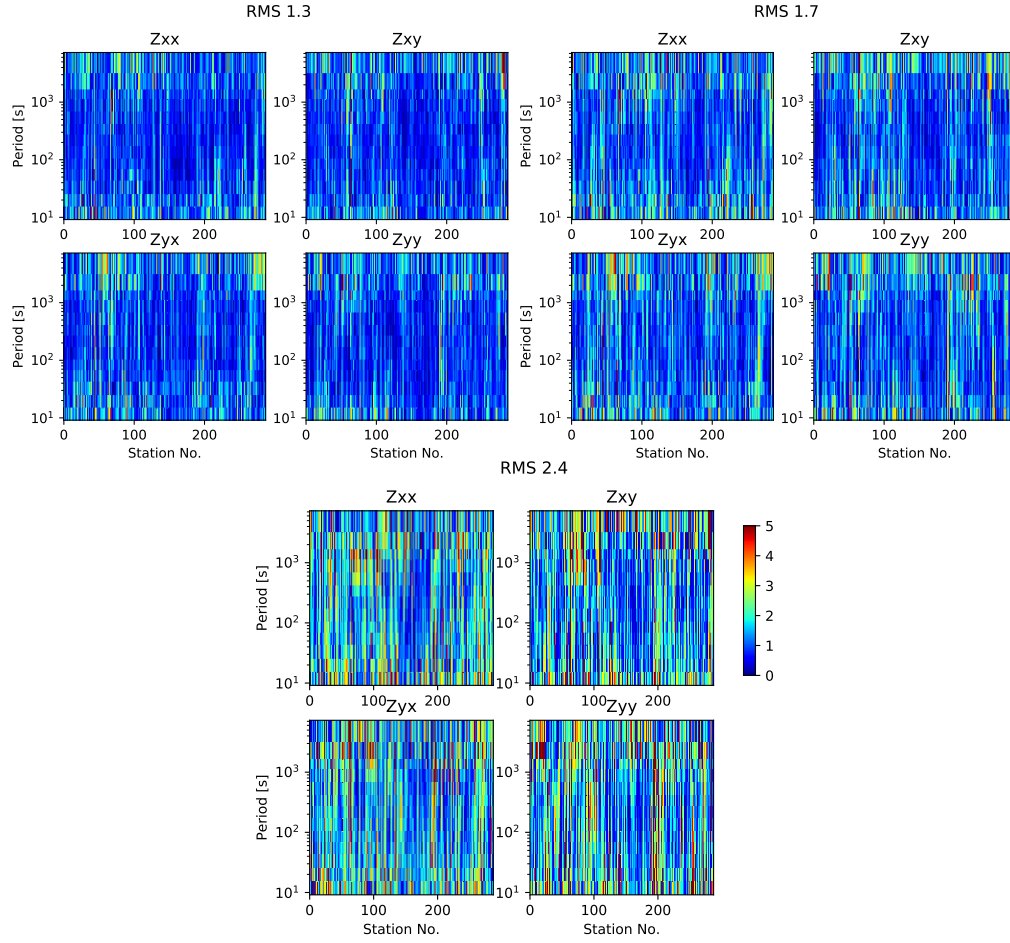
Figure 7: Misfit as a function of station number and period for the individual components of the impedance tensor. The overall data misfit levels are $\Phi = 1.3$ (top left), $\Phi = 1.7$ (top right) and $\Phi = 2.4$ (bottom) as described above.
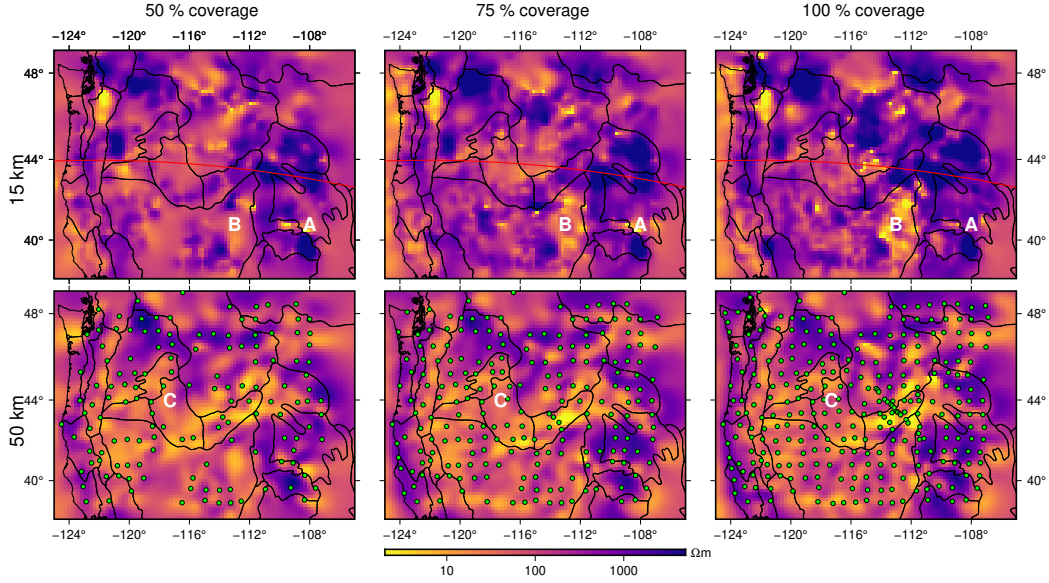
Figure 8: Horizontal slices through the model at 15 km (top) and 50 km (bottom) for different amounts of sites from 50% coverage to full coverage with all available sites (100%). We show sites that were used in the inversion as dots in the lower panel.

The preceding considerations are part of the canon of standard methods used to assess geophysical inversion results and to assess optimal regularization levels, and thus can be found, to varying degree, in well-characterized and fully assessed inversion asessments (e.g., MacCarthy et al., 2011; Rao et al., 2014; Ben Mansour et al., 2018). A densely sampled $\Phi$ versus model "roughness" curve encompassing many models is commonly examined in such studies to estimate a preferred model with optimal trade-off between data misfit and regularization (e.g., Aster et al., 2018).

### 3.1.2. Data Coverage and Model Discretization

A feature that sets USArray apart from many other geophysical data sets at the continental scale is that it encompassed quasi-regularly spaced uniform high-quality stations virtually across the entire conterminous U.S. In contrast, many geophysical field campaigns at large scale have relatively uneven station coverage due to diverse practical challenges (e.g., Evans et al., 2011; Dong et al., 2016; Moorkamp et al., 2019). Here, we show the effects of uneven data coverage on the inversion results for the MT problem. While the general analysis above on noise levels, data fit, regularization, and model assessment above is largely independent of the geophysical method, the following discussion is more method specific. MT is an inductive method and as such each measurement site is sensitive to resistivity variations within a *sensitivity kernel* where model sensitivity to a particular measurement generally decreases with distance from the acquisition site. Therefore, removing one or two stations from a region will alter the inversion model and its resolution, and such a perturbation to the model will generally be lesser for deep or generally more distant model features. When MT data are collected from a spatially well sampled array, "deep" will be approximately on the order of the station separation. Surface wave tomography, gravity, and magnetic inversions, although based on different physics, are similar in having spatially broad sensitivity kernels. Ray theoretical seismic tomography, as a counterexample, has more restrictive (e.g., along-ray-path) sensitivity kernels and may thus show qualitatively different model sensitivities to changes in station geometry.

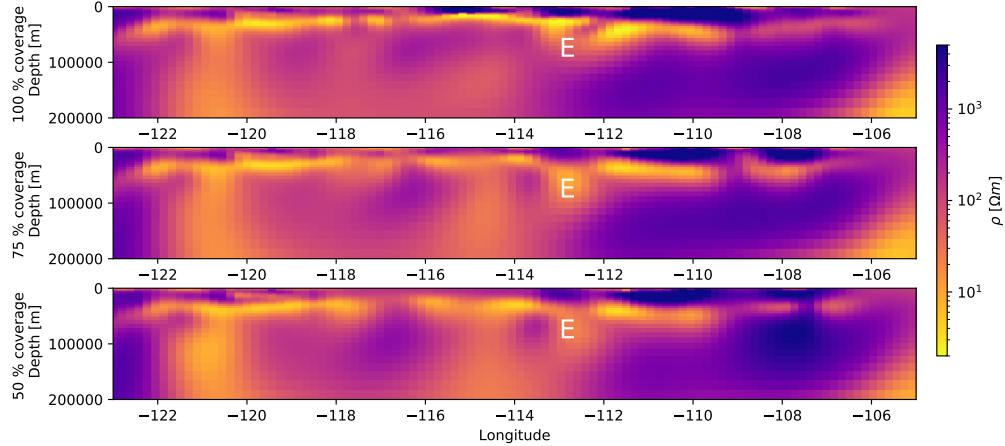To assess the effects of variable station density on the USArray MT in-

Figure 9: Vertical slices along the red line in Figure 8 for 100% coverage (top), 75% coverage (middle) and 50% coverage (bottom).

version, we consider two decimated data sets from the full set of USArray data: one where we randomly remove 25% of the sites, and one where we remove a further 25%, resulting in a net station reduction of 50%. Figure 8 shows the locations of the selected stations for each of these data sets (bottom panel). We invert each of these data sets and $\Phi = 1.7$ to make the inversions comparable in terms of data fit.

We show a comparison of the resulting models in Figures 8 and 9. At first glance the results look surprisingly similar for the three station density levels. However, on closer inspection we can identify some significant differences, particularly in the horizontal slices and at shallow depth (15 km). We will discuss three areas in particular (marked $A$, $B$ and $C$ in Figure 8): At 15 km depth we observe several small conductive structures in region $A$ with 50%

site coverage. These become less pronounced at 75% and disappear virtually completely when we use all sites in the inversion. Comparing the locations of sites included in the inversion, we can see that these features are located near isolated stations and thus primarily included to fit the data at these sites without further constraints.

Region $B$ exhibits one of the biggest gaps in site coverage at 50%. There, the situation is reversed compared to region $A$. With full site coverage we observe a significant conductor with some internal heterogeneity. At lower sites coverage this conductor starts to fade, the resistivity in the region increases, and internal details are lost. Still, we can identify it as a region of enhanced conductivity compared to the surrounding regions. At a depth of 50 km, region $C$ is another area were site coverage changes drastically. Despite this, the changes in the models are relatively small. Close inspection reveals some differences in the absolute value of resistivity and the location of boundaries of more resistive structures, but the differences are surprisingly small given that we incorporate date within a radius of more than 100 km.

The vertical slices (Figure 9) along the red transect in Figure 10 also show illustrative differences. Towards the western end of the profile, structures are very similar, and there only appears to be some minor difference in the thickness of the crustal conductor. The region $E$, though does show more pronounced differences. With full coverage (top panel in Figure 9), we can see a disruption of the crustal conductor and that the eastern limb of the conductor submerges below the western limb, as may be the signature of a major crustal fault. This part of the transect coincides with the eastern limit of Snake River Plain and the transition into the Middle Rocky Moun-
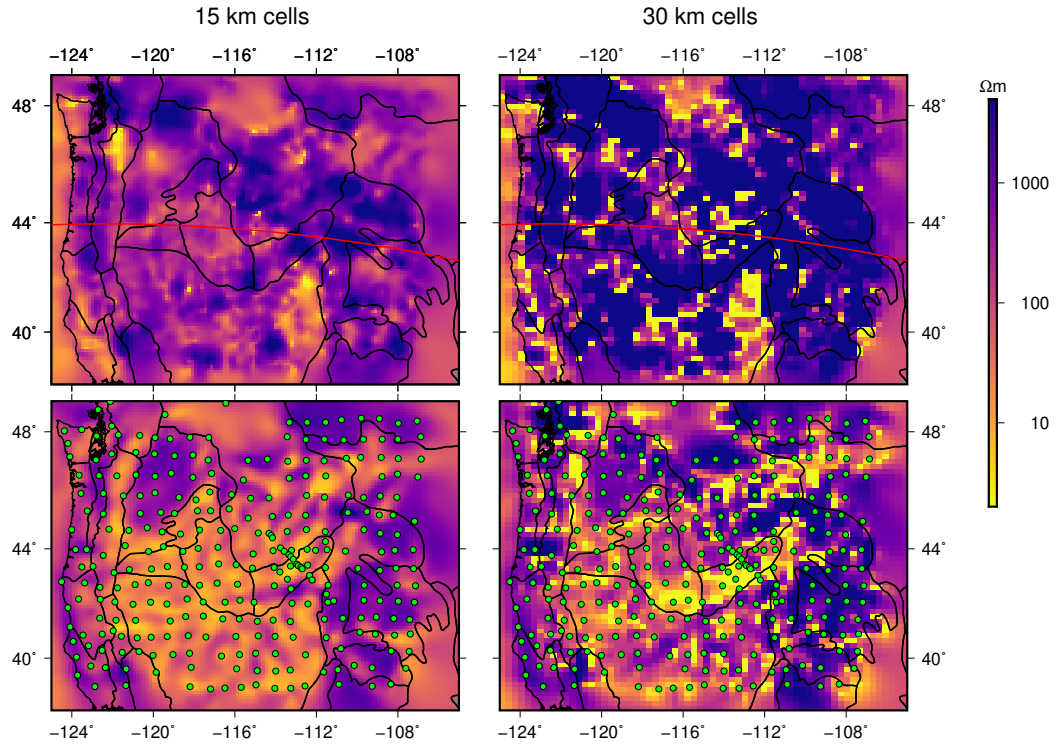
Figure 10: Horizontal slices through the inversion models at depths of 15 km (top) and 50 km (bottom) for two different types of horizontal discretization. The left-hand side uses horizontal cell sizes of 15 km as in the example above, the right-hand side is an inversion with horizontal cell sizes of 30 km.

tains geologic province where strong changes in crustal velocity and density have been observed (DeNosaquo et al., 2009; Yuan et al., 2010). When the station density is reduced (middle and bottom panels), we can still see a trace of the feature, but the geometry seems to be reversed. For both 75% and 50% coverage the eastern limb is now located above the western limb. In the inversion with full station density we have a collection of sites with inter-station distances that are significantly smaller than average. All of these sites are missing in the randomly reduced coverage inversions. For a more complete assessment of the situation we would need to perform resolution tests (e.g., by using idealized faulty resistivity structures, generating synthetic data, and then inverting under identical assumptions) to validate which aspects of the data are sensitive to the geometry of the feature. Still, from these results we can see that with reduced coverage we can still identify many of the significant features, but with decreased coverage the resolution becomes too low to make detailed interpretations of geometric relationships. Note that this station decimation perturbation is depth-dependent and the shallower regions of the model are more affected than the deeper ones, since deeper features of the model are constrained by data at multiple stations in all cases.

We will next discuss relevant effects of model discretization, in this case the dimensions of the cells used to parameterize our model. In our MT modeling and inversion algorithm we partition the subsurface resistivity into constant resistivity rectangular prisms of fixed sizes. While not the only option, this block model parameterization is widely used in geophysical modeling (e.g., Podvin and Lecomte, 1991; Egbert and Kelbert, 2012; Kolawole et al.,
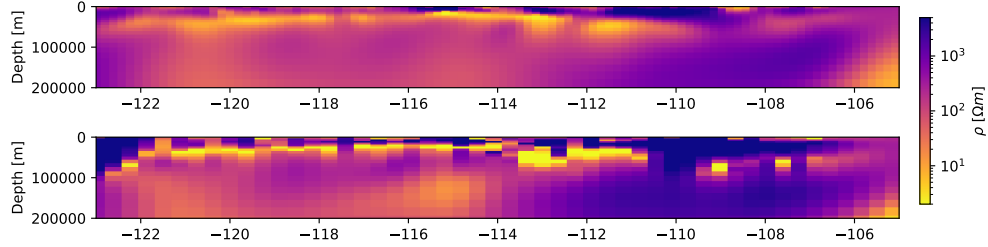
Figure 11: Vertical slices through the inversion model along the red lines in Figure 10 with a horizontal discretization of 15 km (top) and 30 km (bottom).

2017). Changing the block sizes has two effects: i) Larger prisms will stabilize the inversion procedure but will reduce resolution and hence our ability to potentially resolve fine-scale structure. This is the process of regularization by discretization introduced in Section 2.5. ii) More subtly, forward modeling accuracy may become adversely affected by large cell sizes (Podvin and Lecomte, 1991; Avdeev, 2005). Our discretization for the previous inversions (15 km horizontal and 1-20 km vertical, increasing with depth) was chosen to satisfy i) and ii) and also ensure computational feasibility. We now double the horizontal discretization to 30 km. This leaves only 1-2 cells between the measurement sites and pushes the forward modeling algorithm beyond what is recommend for accurate results. The resulting inversion models and the comparison with the finer discretization are shown in Figures 10 and 11.

Interestingly we can fit the observations to the same level of misfit as before. Comparing the models, the first observation is that conductivity contrasts are strongly enhanced with the coarser discretization; with bigger cellsm conductors tend to be more conductive and resistors more resistive

37

than with smaller cells. There are also notable differences in the geometries of these structures and particularly at 15 km the model with a coarse discretization has blocky artefacts. Still, at depth the general qualitative conclusions, i.e., the location of conductors without regard for their absolute conductivity, is similar in both models. For vertical slices (Figure 11), the blocky appearance of the coarsely discretized model is even more apparent. Although we are using all of the stations in the inversion, the crustal scale feature $E$, discussed above, cannot be identified in the coarse discretization. Instead, the model suggests an abrupt change in the thickness of the crustal conductor. Here, we clearly reach the limit of what can be resolved with such large prisms and the algorithm replaces the fine scale changes with something that produces an approximately equivalent synthetic response that obscures the nature of the feature.

Meqbel et al. (2014) performed similar experiments with the same data set but using a somewhat different inversion algorithm (shown in their supplementary material) and the results are also briefly discussed in Miensopust (2017). They report some similar observations, e.g., increased conductivity contrast, but cannot fit the data as well with the coarse mesh. This is likely due to problems with near surface structures that cannot be accommodated in their inversion but their effect is accounted for in our approach (Avdeeva et al., 2015). This also explains why our results are relatively similar at depth, while Meqbel et al. (2014) see some significant differences. This example illustrates the complex resolution interactions that can occur between structures in different parts of the model in inverse problems.

The above experiments have highlighted some issues when performing

three-dimensional inversions of geophysical data for lithospheric structure due to data uncertainty, ill-posedness and imperfect resolution, and station density. Still, with reasonable resolution and assessment of data fit versus model smoothing, most of the first-order structures are stable and we have confidence that they are required by the data and reflect the true Earth structure, albeit with limited resolution. Of course, in many cases we want to move from qualitative comparisons to quantitative statements, particularly when inferring quantities of geological interest such as composition or melt fraction. The following section provides an example on how this critical interpretation step may be approached in a joint inversion context.

## 4. Geophysical Inversions for Physical State

Initial results from geophysical inversion studies are commonly presented as collections of relevant physical parameters (e.g., seismic velocities, electrical conductivity, density) describing properties of the Earth's interior. These parameters are typically subsequently used to make inferences about the physical/thermodynamic state of the Earth (e.g., temperature, pressure, composition) (e.g., Jones et al., 2013). This conversion, however, is never straightforward and requires the formal definition of at least two functional relationships.

The first such relationship is that between the data and the set of governing physical parameters, i.e., the forward problem operator as introduced in Section 2. An important example is the relationship between travel times and seismic velocity structure. In this case, the forward model often incorporates approximations to the full wave propagation physics (e.g., ray theory

assumptions), which may introduce resolution or other artifacts in the results.

The second level of functional relationship is between the set of governing physical parameters (e.g., seismic velocity) and specific physical properties of interest that may include composition, pressure, water content, and temperature. Since this set of fundamental parameters (e.g., temperature) controls the second set of governing physical parameters (e.g., seismic velocity), they are sometimes referred to as the primary and secondary parameters, respectively (e.g., Khan et al., 2011; Afonso et al., 2016a; Fullea, 2017). Such relationships are often multi-valued or ill-posed in regions of the parameter space, thus introducing non-uniqueness and/or noise sensitivity issues. An example is the relationship between seismic travel time observations and elevated temperature and/or partial melt conditions, both of which reduce seismic velocity.

The combined inverse problem described above introduces additional complexity (e.g., the thermodynamic relationship between temperature, pressure, composition and bulk rock seismic velocities) to the net primary-secondary forward operator that now links primary parameters with data. As with many inverse problems, the associated operator $g$ is typically rank deficient, reflecting a nontrivial model null space, and/or ill-posed, indicative of strong model sensitivity to data noise. As elaborated earlier, a solution to these challenges is to incorporate regularization, resolution analysis and testing, and sometimes a strategic choice of parameterization that is particularly relevant to a hypothesis test or other goal.

## 4.1. Integrated Geophysical-Petrological Joint Inversion

Integrated geophysical-petrological approaches utilize a self-consistent framework where jointly estimated secondary parameters of differing types, such as seismic velocities (e.g., Khan et al., 2011), density (e.g., Fullea et al., 2015) or electrical conductivity (e.g., Vozar et al., 2014) are linked by the common subsurface thermochemical conditions via thermodynamic and mineral physics considerations (e.g., Connolly, 2005; Kuskov et al., 2014). Therefore, integrated approaches, both based on forward modelling (e.g., Afonso et al., 2008; Fullea et al., 2009, 2011, 2012) and inversion (e.g., Khan et al., 2006, 2009; Afonso et al., 2013a,b, 2016b), estimate primary parameters such as temperature, bulk composition, water and melt directly from geophysical observations. Here, we briefly summarize and demonstrate via an illustrative lithosphere-scale example the main components in the integrated geophysical-petrological approach. This example includes the basic characterization (e.g., the lithosphere-asthenosphere boundary and mantle geotherm) and the petrological and the mineralogical components (e.g., the thermodynamic framework and mineral physics) of the ensemble primary parameter inverse problem.

## 4.2. The Lithosphere-Asthenosphere Boundary and Mantle Geotherm

The lithosphere-asthenosphere boundary (LAB) defines the lithosphere in terms of its dynamics (rigid outermost lid/plate) and temperature (conductive $V_s$ convective heat transport). Lithosphere and LAB characterizations have been widely presented as inferred from secondary physical parameters, including seismic velocities, seismic and electrical anisotropy, and electrical resistivity (e.g., Eaton et al., 2009). A common approach is to consider the

41

magnitude and vertical gradient of $V_s$ as a proxy for the LAB (e.g., Rychert and Shearer, 2009) although there is no straightforward mapping between seismic parameters and temperature and viscosity given heterogeneous silicate petrology, grain size, the effects of $H_2O$, and other complexities (e.g., O'Donnell et al., 2017). Furthermore, the best choice(s) of the appropriate threshold seismic velocity or gradient for estimating the transition depth from mantle lid to asthenosphere, remain controversial (e.g., Bartzsch et al., 2011). Likewise, the strong electrical conductivity change commonly associated with the LAB could be influenced by multiple factors, i.e., partial melt and/or the presence of relatively small amounts of $H_2O$ (e.g., Karato, 2012; Schmerr, 2012). Seismic receiver function studies show a relatively clear velocity contrast at the LAB for thinner continental crust or oceans (e.g., Rychert et al., 2005; Kawakatsu et al., 2009; Hansen et al., 2015) but the signal is less clear in thick, cratonic terranes (e.g., Eaton et al., 2009; Kind et al., 2012; Foster et al., 2014). Based on the geotherm, the lithosphere can be defined as the portion of the upper mantle where heat conduction is dominant, so that the base of the lithosphere would correspond to the depth of a prescribed isotherm, usually in the range 1250-1330°C. Below such isotherm the low mantle viscosity permits convective processes and vigorous mantle stirring. Hence, the sublithospheric geotherm is customarily described by an adiabatic gradient, generally assumed to be in the range 0.35-0.6° C/km. In this conception, the (thermal) LAB can in principle be described by the intercept of a conductive geotherm and the adiabatic geotherm (e.g., Priestley and McKenzie, 2006). An alternative description is to define a thermal buffer/transitional layer connecting the convective and

adiabatic domains where heat transfer is controlled by both conduction and convection mechanisms(Afonso et al., 2008; Fullea et al., 2009). The boundary of the mechanical lithosphere or stagnant lid will be in the vicinity of the thermally defined lithosphere but its location will be dictated by both pressure (depth) and by minor mantle components that influence viscosity.

### 4.3. Thermodynamic Framework and Mineral Physics

Earth's mantle compositional space is usually defined within the major oxide system CaO-FeO-MgO-$Al_2O_3$-$SiO_2$ (CFMAS) or $Na_2O$-CaO-FeO-MgO-$Al_2O_3$-$SiO_2$ (NCFMAS). The NCFMAS system accounts for >98 wt. % of the crust and mantle and is thus considered to be an excellent starting basis for modeling mineral phase assemblages. The NCFMAS space can be treated as six independent variables specifying the weight proportion of each of the major oxides) (e.g., Afonso et al., 2008; Fullea et al., 2015) or as a single-parameter basalt-harzburgite mixture with either a chemically equilibrated bulk composition (e.g., Khan 2016) or as a mechanical mixture of the basaltic and harzburgitic end-members (Xu et al., 2008). Other authors have shown that the number of independent oxides in geophysical applications can be effectively reduced to one or two (e.g., Afonso et al., 2013a).

From a chemical standpoint, the lithospheric mantle is thought to be primarily peridotitic, with olivine being the volumetrically dominant mineral phase (>40%). Mantle peridotite composition is generally characterized according to fertility, i.e., enrichment in the basaltic component that relates to melt extraction. The more refractory or infertile the peridotite, the more the $SiO_2$-, CaO- and $Al_2O_3$-enriched melt phase has been extracted, leaving an MgO-enriched solid residue. A commonly used fertility index is the

magnesium number (Mg#=MgO/(MgO+FeO)). The Mg# of a perdotite increases almost linearly with the amount of melt extraction (e.g., Herzberg, 2004). The sub-lithospheric mantle is thought to be more fertile than the lithospheric mantle (where greater melt extraction has generally occurred).

Under the assumption of thermodynamic equilibrium ($T > 500°C$) stable mantle mineral assemblages can be determined using a Gibbs free energy minimization approach (e.g., Connolly, 2005, 2009) using thermodynamically self-consistent databases (e.g., Stixrude and Lithgow-Bertelloni, 2005, 2011; Ricard et al., 2005; Matas et al., 2007; Piazzoni et al., 2007), and bulk secondary physical parameters can be estimated using constituent elastic moduli, electrical conductivity and density of the stable end-member minerals (e.g., Connolly and Kerrick, 2002; Afonso et al., 2008; Fullea et al., 2011). In the case of seismic velocities, partial melt and anelasticity effects are highly relevant, especially at high temperatures (e.g., Karato, 1993; Sobolev et al., 1996; Goes et al., 2000; Cammarano et al., 2003). Recent laboratory studies detect a decrease in shear wave velocity ($V_s$) and shear wave attenuation ($Q_s$) of up to 50% and an order of magnitude, respectively, for a melt fraction of 4% (Chantel et al., 2016). Furthermore, experimental studies suggest a progressive, $V_s$-decreasing effect of anelasticity below the solidus temperature (e.g., Yamauchi and Takei, 2016; Takei, 2017). Water plays a major role in the electrical conductivity of minerals through proton conduction from different chemical species within the crystal lattice and at grain boundaries (c.f., Fullea, 2017, and references therein). In spite of controversial experimental results (e.g., Karato and Dai, 2009; Yoshino, 2010) there is a consensus in that water considerably increases electrical conductivity of nominally an-

hydrous minerals. A further factor that can potentially enhance electrical conductivity of upper mantle minerals is interconnected melt (e.g., Gaillard, 2004; Tyburczy and Waff, 1983; Ni et al., 2011; Miller et al., 2015). Overall, the effective conductivity of a partially molten rock depends on the melt fraction and the conductivities of the bulk rock and melt, with different mixing rules connecting the bulk rock and the melt being proposed in the literature (e.g., Waff, 1974; Glover, 2010; Laumonier et al., 2017).

## 4.4. Case Study: The Physical State of the Wyoming Craton and Northern Basin and Range, North America

We illustrate some of the issues related to integrated geophysical-petrological modelling of the lithospheric structure. For the sake of simplicity, we will restrict the input data here to fundamental mode Rayleigh and Love seismic surface waves), topography and heat flow, i.e., data that can be usefully modelled following a 1-D approach. Surface wave phase velocity dispersion curves are sensitive to vertical seismic velocitie profiles ($V_p$, $V_s$), density and seismic attenuation ($Q$). The surface elevation, under the local isostasy assumption, depends on the vertically integrated crustal and lithospheric mantle densities, whereas surface heat flow depends on the crustal structure (radiogenic production, thermal conductivity, thickness) and thermal lithospheric thickness (c.f., Afonso et al., 2008; Fullea et al., 2009).

Our data include phase-velocity dispersion curves from global surface phase-velocity maps estimate by the Automated Multimode Inversion (AMI) (Lebedev et al., 2005) of seismic waveforms. AMI incorporates earthquake recordings from 6242 stations (including EarthScope USArray) and 25496 events worldwide (Schaeffer and Lebedev, 2013; Celli, 2020). Fundamental

mode phase velocities are inverted for maps at 98 different periods in the 10-460 s range, with a logarithmic sample-interval increase, and accounting for azimuthal anisotropy. The lateral resolution averages 225 km over a triangular grid. Data redundancy is exploited via a posteriori outlier rejection to reduce the impacts of measurements errors on the phase-velocity maps. The relative uncertainties estimated for the phase velocities are 0.3 % for periods < 20 s, 0.2% for periods 20-50 s, 0.2-0.5% for periods 50-200 s, and 0.5% for periods > 200 s.

Seismic attenuation is included as a posteriori correction to anharmonic velocities computed using thermodynamic arguments (e.g., Minster and Anderson, 1981; Karato, 1993; Fullea et al., 2012) using

$$V_p = V_{p0}(T, P) \left[ 1 - \left( \frac{2}{9} \right) \cot \left( \frac{\pi \alpha}{2} \right) Q_s^{-1} \right] \tag{27a}$$

$$V_s = V_{s0}(T, P) \left[ 1 - \left( \frac{1}{2} \right) \cot \left( \frac{\pi \alpha}{2} \right) Q_s^{-1} \right] \tag{27b}$$

$$Q_s^{-1} = A \left[ T_0 \, d^{-1} \exp \left( \frac{-E + VP}{RT} \right) \right]^\alpha \tag{28}$$

$$Q_p^{-1} = (4/9) Q_s^{-1} \tag{29}$$

and assuming an infinite quality factor for the bulk modulus, i.e., $Q_K^{-1} \to 0$. $V_{P_0}$ and $V_{S_0}$ are the unrelaxed high frequency anharmonic velocities at a given temperature ($T$) and pressure ($P$) and bulk composition. $A = 750$ s$^{-\alpha}$ $\mu$m$^\alpha$ for the empirically-determined exponent $\alpha = 0.26$ (Jackson et al., 2002), $R$ is the universal gas constant, $d$ is the grain size, $E$ is the activation energy, $V$ the activation volume, and $T_0$ is a reference period. To minimize the impact of uncertainties in $Q_s$ on the $V_s$ vs. phase velocity relationship, our seismic velocity profiles have a reference period (50 s) that is in the middle

of the frequency range used in this study (Liu et al., 1976; Lebedev and Van Der Hilst, 2008). Mantle grain size is controlled by the trade-off between crystal growth (increased $d$) and recrystallization (decreased $d$) and remains substantially uncertain. Measurements of $d$ from mantle xenoliths are in the range 3-10 mm (e.g., Karato, 2008) but may be affected by deformation during the exhumation process. The effects of melt on seismic velocities and $Q$ are computed according to the experimental model of Chantel et al. (2016) and Hammond and Humphreys (2000). The mantle melt fraction represents a typical example of a parameter that contributes to the inversion ill-posedness as characterized earlier in this paper. Small changes in melt fraction produce a large effect on seismic velocities and attenuation, and, therefore, on predicted surface wave phase velocities to be matched against data during the modeling procedure. Furthermore, available laboratory results measuring melt effects on seismic velocities differ, and this contributes to the uncertainties in the output parameters. To mitigate ill-posedness here, we include a near-solidus pre-melt contribution (e.g., Yamauchi and Takei, 2016; Takei, 2017) to linearly smooth out the effect of melt on attenuation over a temperature range in the neighborhood of the solidus (Bonadio et al., 2018). We assume that the mantle peridotitic dry solidus and liquidus from Katz et al. (2003) and references therein to estimate melt fraction. In this way we do not explicitly include melt fraction as an inversion parameter but implicitly account for it through the mantle geotherm and solidus curve.

We use two illustrative locations from differing tectonic provinces: the Wyoming craton (WC) and the North Basin and Range terrain (NBR) (Figure 2). The average topography, surface heat flow and Moho depth data are

| Column | Elevation | Surface heat flow | Moho depth |
|---|---|---|---|
| Wyoming craton (WC) | 1.9±0.2 km | 60±15 mW/m$^2$ | 43.4±4.4 km |
| North Basin and Range (NBR) | 1.4±0.1 km | 70±10 mW/m$^2$ | 31.2±4.6 km |

Table 1: Data and prior Moho depth with uncertainties for the integrated geophysical-petrological inversion case study. For locations corresponding to the two columns see the two blue stars in Figure 2

listed in Table 1. The Moho depths are taken from the global CRUST1.0 model (Laske et al., 2013) with uncertainties estimated by Szwillus et al. (2019) based on geostatistical interpolation of controlled source seismic data from the U.S. Geological Survey [USGS] Global Seismic Catalog [GSC] database (Mooney, 2015). In Fig. 12 we show the Rayleigh and Love surface wave phase velocity data used in this study. Synthetic phase velocity dispersion curves are computed using a version of the MINEOS code (Masters et al., 2011) assuming the ak135 reference model for depths > 400 km (Kennett et al., 1995).

We define our model space in terms of primary parameters: temperature and composition of the lithosphere and upper mantle. Our fundamental variable is the thickness of the lithosphere, $Z_{\mathrm{LAB}}$, here defined as the 1300°C isotherm, and also as the chemical boundary between the lithosphere and the underlying sublithosphere. The temperature within the lithosphere is estimated by solving the 1-D heat conduction steady state equation in a model domain defined by the fixed temperature boundary conditions at the surface topography and the LAB depth (Fullea et al., 2012). The inclusion of the heat conduction equation imposes an additional level of (physical) regularization in our inversion regarding the seismic velocity gradient with depth.
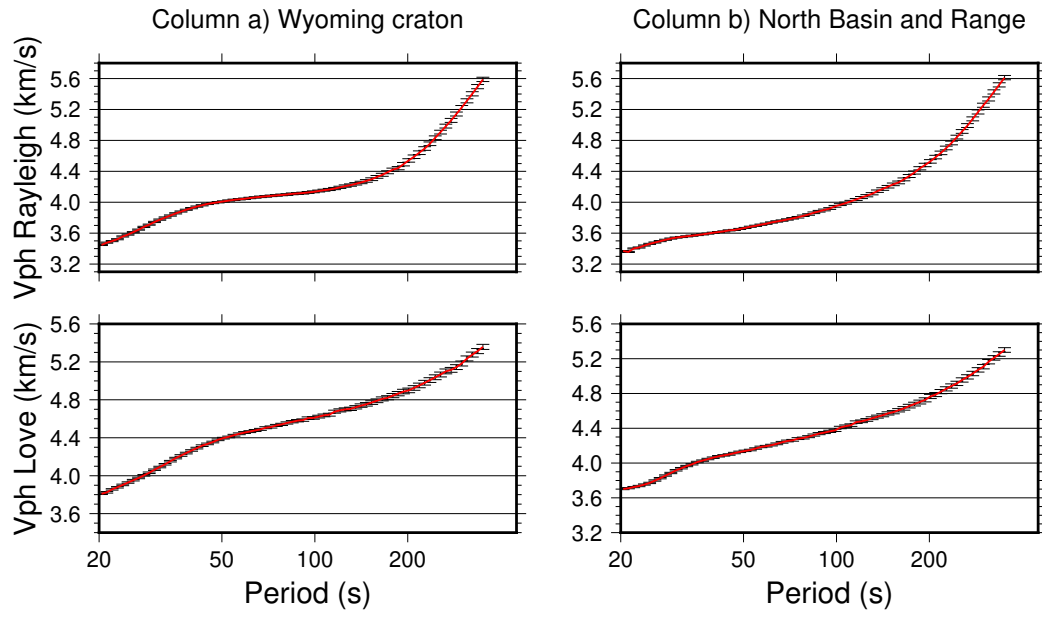
Figure 12: Rayligh (top) and Love (bottom) surface wave dispersion phase velocity curves used as input data in the inversion for physical state in this study. Left and right plots correspond to lithospheric columns WC and NBR respectively (Table 1; Figure 2).

Below the lithosphere we invert for a thermal buffer of variable thickness (<50 km) transitioning the thermal lithosphere to the adiabatic (convective) mantle. The adiabatic mantle is parameterized by the temperature at three equally spaced depths from the base of the thermal buffer (assumed to be $T_{\text{buff}} = 1400°C$) to the top of the transition zone at 400 km. Sublithospheric temperatures are vertically regularized depending on the lithosphere and thermal buffer thickness by constraining the excursion from a reference adiabatic gradient of 0.5° C/km (only departures $\leq 100°C$ are allowed). The chemical parameter space is defined in terms of the bulk amount of $Al_2O_3$ in two domains of lithosphere and sublithosphere. CaO-MgO major oxides are assumed to be correlated to $Al_2O_3$ based on global petrological data bases (Afonso et al., 2013a, and references therein), using

$$MgO = 49.369 - 4.106 \cdot Al_2O_3 + 0.3438 \cdot (Al_2O_3)^2 \tag{30}$$

$$CaO = -0.164 + 0.90 \cdot Al_2O_3 \tag{31}$$

and FeO is fixed (Table 2). We also invert for: i) crustal structure as three layers of variable thickness defined by $V_s$ and density; and ii) radial crustal anisotropy at 56, 80, 110, 150, 200, 260, 330, and 400 km depth within the mantle. The Moho depth is allowed to depart from the reference/prior value from CRUST1.0 within the uncertainties estimated by Szwillus et al. (2019). Crustal P-wave velocities are computed from the $V_s$ using fixed Poisson ratios (or equivalently, $V_p/V_s$) (Table 2). Radial anisotropy is here defined as:

$$\phi = \frac{V_{sh} - V_{sv}}{V_s} \tag{32}$$

where

$$V_s = \frac{2V_{sv} + V_{sh}}{3} \tag{33}$$

50

| Fixed parameter | value |
| --- | --- |
| Thermal conductivity crust | 2.2/2.5/2.1 W/(m °K)* |
| Vp/Vs | 1.75/1.75/1.81* |
| Crustal radiogenic production | 0.9 $\mu$W/m2 |
| Mantle radiogenic production | 0.01 $\mu$W/m2 |
| FeO lithosphere | 8.1 wt% |
| FeO sublithosphere | 8.05 wt% |
| LAB temperature | 1300°C |

Table 2: Fixed parameters in the geophysical-petrological inversion case study. *Values separated by "/" correspond to the upper/mid/lower crustal layers.

and $V_{sv}$, $V_{sh}$ and $V_s$ are the are velocities of the vertically and horizontally polarized S waves respectively, and $V_s$ is the Voigt isotropic average ($V_p$ is assumed to be isotropic). Anisotropy represents an example of ill-posedness in our forward problem since stratified models alternating strongly positive and negative anisotropic layering often can fit the data essentially as well as more physically realistic smooth varying models. We therefore regularize the problem by minimizing the solution 2–norm difference with respect to a smooth isotropic reference model in the objective function.

The inversion is framed into a non-linear least squares problem and thus lies within the field of the classical deterministic inversion perspective as defined in Section 2. We minimize an objective function that is a nonlinear generalization of (19)

$$[\mathbf{g}(\mathbf{m}) - \mathbf{d}]^T \mathbf{C}_D^{-1} [\mathbf{g}(\mathbf{m}) - \mathbf{d}] + [\mathbf{m} - \mathbf{m}_{\mathrm{ref}}]^T \mathbf{C}_M^{-1} [\mathbf{m} - \mathbf{m}_{\mathrm{ref}}]) \qquad (34)$$

where $\mathbf{g}(\mathbf{m})$ is the nonlinear forward model operator that implements the in-

tegrated geophysical-petrological modelling approach described above. The left-hand term in (34) is a quadratic form corresponding to the square of the weighted data misfit 2–norm that takes into account data uncertainties. $\mathbf{C}_D^{-1}$ and $\mathbf{C}_M^{-1}$ are inverse observational and model covariance matrices respectively, here assumed to be diagonal. The right-hand quadratic form term in (34) regularizes the problem. $\mathbf{C}_M^{-1}$ is a diagonal matrix of squared weighting factors for the respective elements of the reference (and regularizing) model vector, $\mathbf{m}_{\mathrm{ref}}$, where the magnitudes of the diagonal elements in $\mathbf{C}_M^{-1}$ control the manner in which the weighted model 2–norm $\mathbf{C}_M^{-12}(\mathbf{m} - \mathbf{m}_{\mathrm{ref}})$ is small. $\mathbf{d}$ is the data vector containing the surface elevation, heat flow, and observed phase velocity dispersion curves for Rayleigh and Love waves measured at 73 periods between 20 and 350 s. For the crustal parameters (velocity, density, thickness), radial anisotropy, lithospheric thickness and mantle composition the regularization term is explicit. In addition, there is an implicit regularization in the way the geotherm is modelled: thermal steady state in the lithosphere (heat conduction domain) and adiabatic gradient(s) in the sublithosphere (heat convection domain). Finally, the linearized pre-melt anelastic parametrization in the vicinity of the solidus described above adds further smoothing to the solution. The nonlinear system of equations is iterative solved using the Levenberg-Marquardt approach.

In the absence of regularization, it is common in solving ill-posed problems to encounter model parameters that are nonphysical and outside of the domain of the joint geophysical-petrological forward problem solver. Our parameter space is heterogeneous in that it includes composition, temperature, thickness, seismic velocities, and density. This raises the characteristic

joint inversion problem of choosing the most suitable $\mathbf{C}_M$ coefficients in the regularization term for the differing data types.

Finding an optimal balance between data fit and regularization/resolution can be a complex task that will vary from study to study depending on the noise characteristics, model parameterization, and the regularization conditions. Here, we adopt a trade-off curve strategy where we begin from a high level of homogeneous regularization in the iterative nonlinear inversion (i.e., constant and high value $\mathbf{C}_M$ coefficients) and progressively reduce it for the different parameter types guided by the value of $\mathbf{m} - \mathbf{m}_{\mathrm{ref}}$ after each inversion. For instance, if for a given post-inversion parameter the associated element of $\mathbf{m} - \mathbf{m}_{\mathrm{ref}}$ is greatly increased as a result of reducing its $\mathbf{C}_M$ (parameter variance) coefficient, in the next iteration the regularization coefficient for that term is re-scaled and kept constant thereafter. For each inversion run defined by a set of $\mathbf{C}_M$ coefficients we then calculate the 2–norm of weighted data misfit (i.e. left hand term in (34)) and the solution distance to the reference model (the 2–norm of $\mathbf{m} - \mathbf{m}_{\mathrm{ref}}$ (i.e. right hand term in (34)). The preferred models were selected based on a criterion of jointly minimizing both the data misfit and the distance to the reference model so that the values of the two quadratic terms in (34) for the preferred solution fall in the knee of the trade-off curve between the two.

Inversion results are shown in Figures 13 and 14. The lithospheric thicknesses under WC and NBR columns are 145-160 km and 65-67 km respectively. The Moho depth is less than CRUST1.0 in WC (39.3-40.7 km) and is greater in NBR (32.3-34.8 km).The lithospheric mantle composition is found to be relatively fertile in the two columns, and slightly more so in NBR

(Mg# =89.26-89.65) compared to WC (Mg# =89.54-89.79). The sublithospheric mantle composition departs little from the reference model. Radial anisotropy is negative or slightly positive in the crust and strongly positive in the first 100 km of the mantle both in WC and NBR columns (Figs. 13 and 14). Below 100 km there is zone of negative anisotropy ($V_{sv} > V_{sh}$; (32)) that in the case of WC overlaps with the lowermost lithospheric mantle and lithosphere-asthenosphere thermal boundary to about 200 km depth. In NBR the zone of negative anisotropy is entirely within the sublithosphere and extends down to 150-170 km depth. Below the negative anisotropy zone there is again another region of mildly positive anisotropy that tends to zero at the mantle transition zone (410 km).

Anelasticity has an important influence on these inversions, especially at high temperatures and in the vicinity of the thermal LAB. To explore uncertainties associated with attenuation modelling we considered a comprehensive range of values for the main physical parameters based on different laboratory experiments and geophysical models (e.g., Faul and Jackson, 2005; Jackson and Faul, 2010; Fullea et al., 2012; Priestley and McKenzie, 2013): 403-440 kJ/mol, 7.8-20 cm$^3$/mol, and 1-30 mm for activation energy ($E$) and volume ($V$), and grain size ($d$), respectively, as described in (28). Taking the predicted attenuation values as a criterion we group the models into three general categories: high, low, and reference attenuation (Figures 13 and 14). High attenuation models are characterized by small grain size and low activation energy and volume; low attenuation models are defined by large grain size and high activation energy and volume; we term as reference models those that are in between the high and low attenuation end mem-

ber models, and that show values comparable to other seismically derived radial attenuation models, e.g., QL6 (Durek and Ekström, 1996), QR19 (Romanowicz, 1995) or QMU3b (Selby and Woodhouse, 2002). The inversion results show that the group of reference and low attenuation models tend to predict consistent lithospheric/upper mantle models that match the constraining geophysical data in the inversion. High attenuation end member models, on the other hand, predict comparatively different models (in terms of lithospheric thicknesses in the case of WC, sublithospheric temperatures and anisotropy in the two cases) that show significantly higher data misfits (Figures 13 and 14). In particular, high shear wave attenuation and its effect on $V_s$ cannot be compensated by changes in other model parameters in our joint inversion approach (i.e., conductive and adiabatic geotherms, thermodynamically constrained seismic velocities, and densities). In the case of the NBR column $V_s$ experience a sharp drop in the vicinity of the LAB (Figure 14). This is due to lithospheric geotherm crossing or approaching the (dry) solidus, with associated melt or pre-melt shear-wave anelasticity.

Several experimental studies have estimated the anelastic effect of melt on seismic velocities (Hammond and Humphreys, 2000) and $Q_s$ (Chantel et al., 2016). The geometry of interstitial melt is uncertain, and alternative models have been proposed, ranging from triple junction tubular structures to randomly-oriented ellipsoidal melt inclusion model or organized cuspate films (e.g., Hammond and Humphreys, 2000, and references therein). In Fig. 15 we show inversion results for differing melt anelastic laboratory-based parameterizations and melt geometries. For comparison purposes we also plot an inversion with no melt-related anelasticity. The inverted thermal
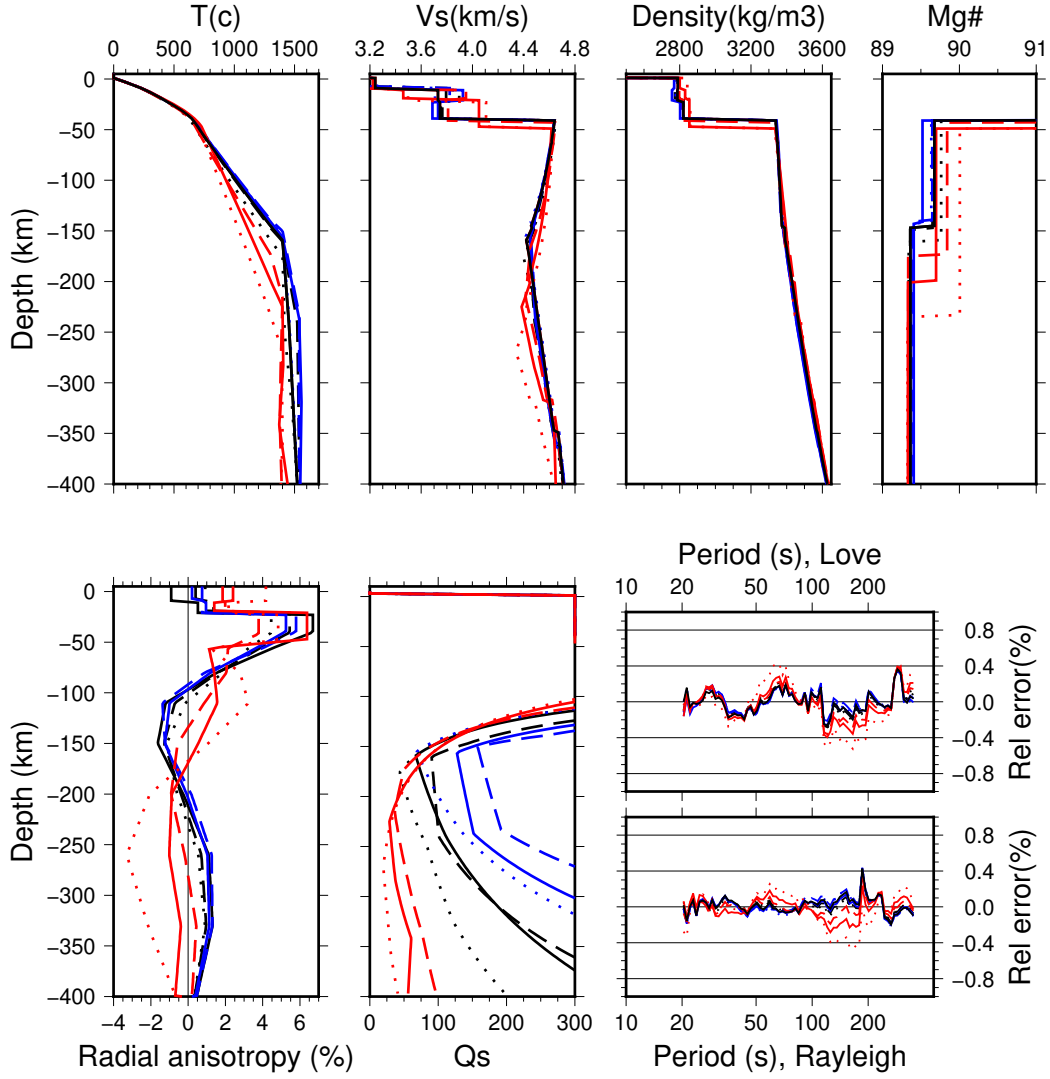
Figure 13: Results of the inversion for physical state in column WC (Table 1). Top row, from left to right: Geotherm, shear wave isotropic velocity, density, and magnesium number. Bottom row, left: radial anisotropy and attenuation. Bottom row, right: residuals (calculated minus observed) for Rayleigh and Love dispersion curves. Black, red and blue lines correspond to reference, high and low attenuation models respectively, as described in the text. Dotted, solid and dashed lines correspond to models with mantle grain sizes of 1, 10, and 30 mm respectively.
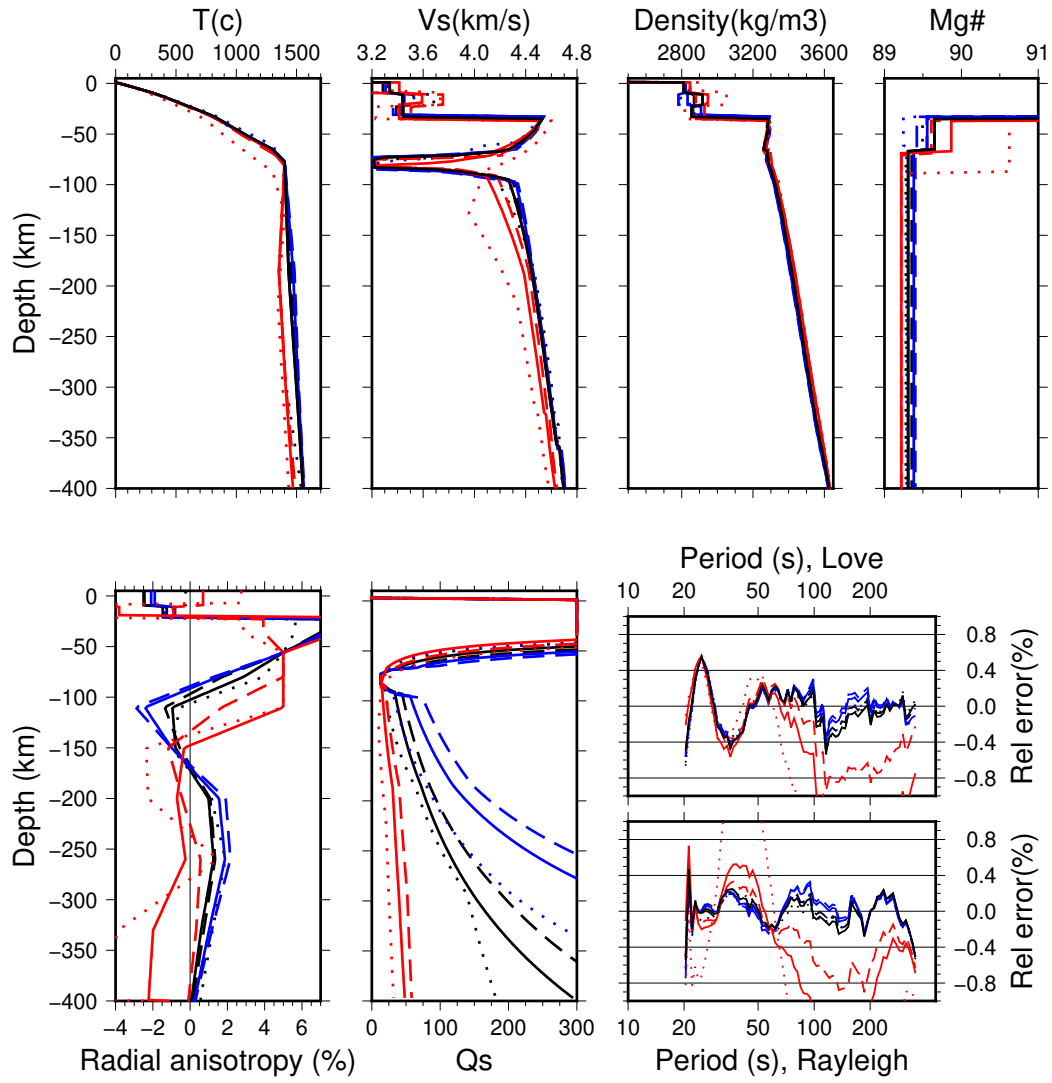
Figure 14: Results of the inversion for physical state in Column NBR (Table 1). See caption in Fig. 13 for description

and compositional mantle models accounting for melt anelasticity fit well the input data and are all very similar except in terms of crustal velocities and radial anisotropy. In contrast the melt-free model is not able to satisfactorily fit the constraining data within the imposed physical regularization in our approach. In the latter case, the inversion pushes the LAB upwards to fit low input surface wave phase velocities via temperature increase, but no physically meaningful value can be obtained. Therefore, we can conclude that the physical regularization in our inversion approach requires independently derived additional mineral physics constraints (i.e., anelasticity effects) to fit the input seismic data. Our results also show that accounting for the uncertainties arising from different experimental results and/or different melt inclusion geometries in the physical description of seismic attenuation does not compromise lithospheric thermochemical model consistency.

### 4.4.1. Uncertainty and resolution

Assuming Gaussian statistics for the data and model spaces, and for local linearization, the model covariance matrix for the solution that minimizes (34) can be calculated as generalization of (21) (Tarantola, 2005)

$$\tilde{\mathbf{C}}_M = \left(\mathbf{J}^T \mathbf{C}_D^{-1} \mathbf{J} + \mathbf{C}_M^{-1}\right)^{-1} \tag{35}$$

where $\mathbf{J}$ is the Jacobian matrix (the matrix of partial derivatives of data elements with respect to model parameters) evaluated at the solution model, $\mathbf{m}$, which has elements given by

$$J_{ij} = \frac{\partial \mathbf{g}(\mathbf{m})_i}{\partial m_j} \ . \tag{36}$$

(35) will not in general be diagonal, even if $\mathbf{C}_D$ and $\mathbf{C}_M$ are. The comparison of the pre-inversion ($\mathbf{C}_M$) (prior) and post-inversion ($\tilde{\mathbf{C}}_M$) (posterior)
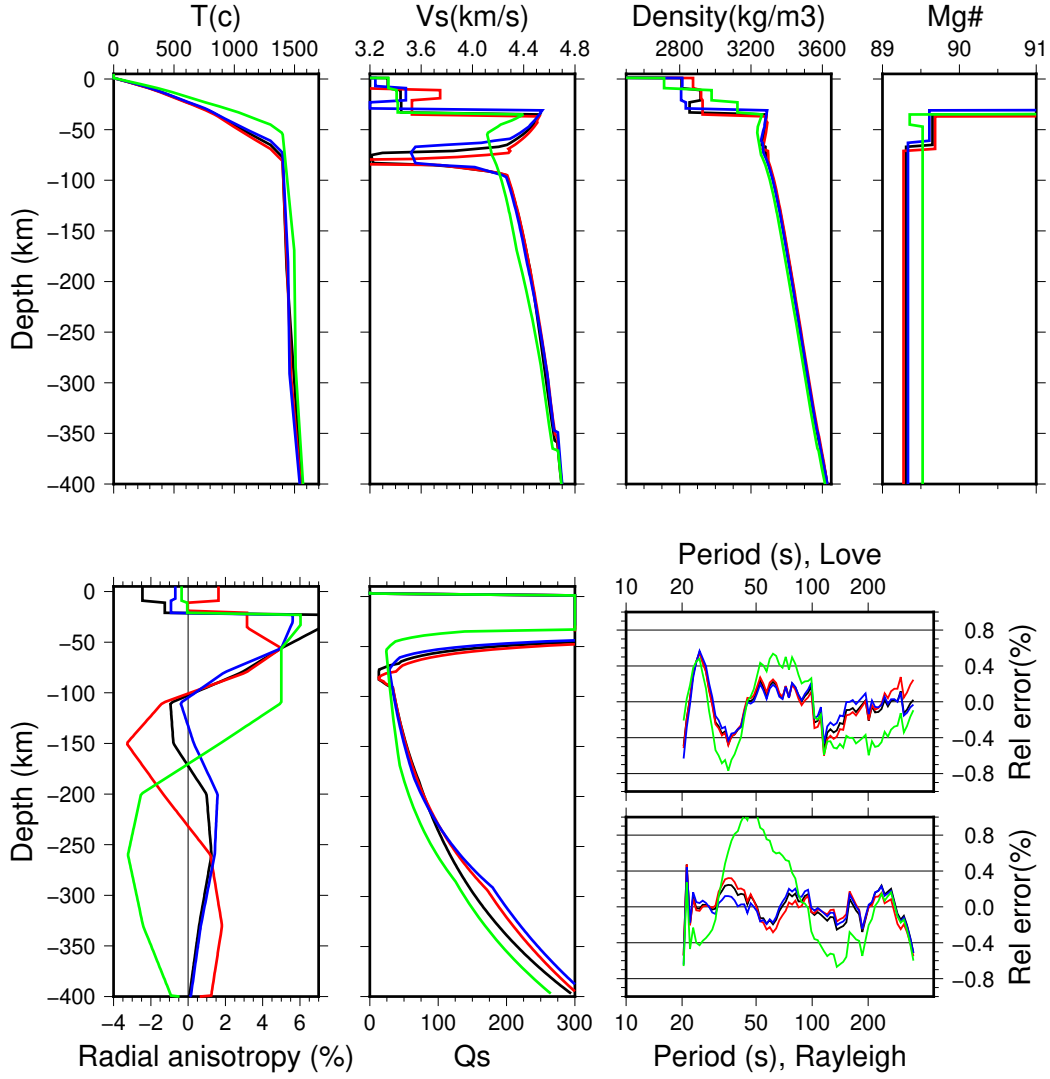
Figure 15: Effect of mantle melting in Column NBR (Table 1). Top row, from left to right: geotherm, shear wave isotropic velocity, density, and magnesium number. Bottom row, left: radial anisotropy and attenuation. Bottom row, right: residuals (calculated minus observed) for Rayleigh and Love dispersion curves. Black lines are models inverted following the experimental results of Chantel et al. (2016). Red and blue lines correspond to models according to the experimental results of Hammond and Humphreys (2000) for triple junction tubular and organized cuspate films interstitial melt geometries respectively. Green lines correspond to a comparison model where no melt attenuation effects are included.

59

model variance and covariances in this formalism provides us with a useful method of estimating how consistently the model parameters have been recovered by the input data, parameter correlations, and for assessing the influence of regularization imposed in (34). If elements are $\tilde{\mathbf{C}}_M$ not reduced relative to $\mathbf{C}_M$, then the corresponding model parameters, rather than being constrained by the input data, are substantially being controlled by the reference model through regularization, and the inversion has not resulted in an appreciable refinement of these parameters. The corresponding model variances, given by the square root of the diagonal elements of $\tilde{\mathbf{C}}_M$, are representative of the inversion uncertainties subject to the choice of the reference model uncertainties in $\mathbf{C}_M$. Note that this evaluation of regularized stochastic model uncertainty, as biased by $\mathbf{C}_M$ using the objective function form of (34) is a complement to the model resolution testing approaches described in Section 2.

A useful object that can be derived from $\tilde{\mathbf{C}}_M$ is the correlation matrix, $\mathbf{C}$, which has elements given by (e.g. Tarantola, 2005)

$$C_{ij} = \left( \frac{\tilde{C}_{M_{ij}}}{\sqrt{\tilde{C}_{M_{ii}} \tilde{C}_{M_{jj}}}} \right) ; -1 \geq C_{ij} \leq 1 \tag{37}$$

Model element pairs with indices $i$ and $j$ and $C_{ij}$ values near to 1 or -1 are strongly correlated or anti-correlated, respectively. In such cases, data are unable to constrain the two parameters independently but, in the limit of $|C_{ij}| = 1$, only a linear combination of them.

In our case study we observe that the largest variance reductions from $\mathbf{C}_M$ to $\tilde{\mathbf{C}}_M$ correspond to the LAB and Moho depths, which had relatively wide reference model variances (Fig. 16). The LAB depth, in particular, is the

60

best resolved parameter by far since it indirectly controls (via temperature distribution within the lithosphere and adiabatic sublithopheric gradients) the values of many parameters throughout the whole column. Crustal seismic velocities and radial anisotropy are also relatively well constrained by the joint inversion of Rayleigh and Love surface wave phase velocities, which are primarily sensitive to the vertically and horizontally polarized components of the shear velocity respectively.

Sublithospheric temperatures are generally poorly constrained, particularly for WC (Fig. 13). For NBR the shallowest sublithospheric temperatures ($<$ 100 km) are comparatively better resolved because for shallow lithospheres the sublithospheric layer is thicker and has more influence on the predicted surface wave velocities (Fig. 14). Similarly, sensitivity to lithospheric mantle composition is more important in the WC column, by virtue of the thicker lithospheric mantle compared to NBR. The situation is reversed for the sublithospheric mantle composition where the largest (yet modest) sensitivity lies in NBR column. Mantle composition constraints are relatively weak. Mantle composition significantly affects density and, therefore, the isostatic mass balance at lithospheric scale and the predicted surface elevation, but have only a mild effect on anharmonic seismic velocities, which are however strongly controlled by temperature variations (e.g., Schutt and Lesher, 2006). In addition, density has a relatively minor effect on surface waves phase velocities. The relatively high uncertainties for composition in our inversion can be understood in the light of the dominant weighting of surface wave seismic data extending over a range of periods, mostly sensitive to seismic velocity variations, compared to surface elevation data (a single

measurement). We observe a strong anti-correlation in the mantle radial anisotropy indicating that the inversion is not able to independently constrain all the vertical nodes in our discretization, which is an expression of rank deficiency (Fig. 17) noted earlier. To different degrees the lithospheric thickness is correlated with Moho depth and shallow sublithospheric temperature, and anti-correlated with the thickness of the buffer thermal layer at its base, and with mantle composition. Furthermore, there is a strong anti-correlation among the crustal $V_s$ values, $V_s$ and crustal anisotropy, and a clear trade-off between the lower crustal $V_s$ and Moho depth. It must be kept in mind that in our study the crustal physical properties (seismic velocities, density) are not thermodynamically constrained but are free to vary independently. Lithospheric mantle composition is moderately anti-correlated with crustal density, reflecting the isostatic balance included in the inversion via surface topography data fitting.

## 5. Summary and Conclusions

Geophysical inverse problems present formidable challenges related to ill-posedness and limited resolution. However, these issues can be usefully overcome by imposing regularization constraints and through informed choices in parameterization and experiment design. The two case studies presented in Sections 3 and 4 demonstrate practical aspects of the fundamental mathematical concepts introduced in Section 2, and are representative of current inversion approaches to investigate the structure of the lithosphere-asthenosphere system

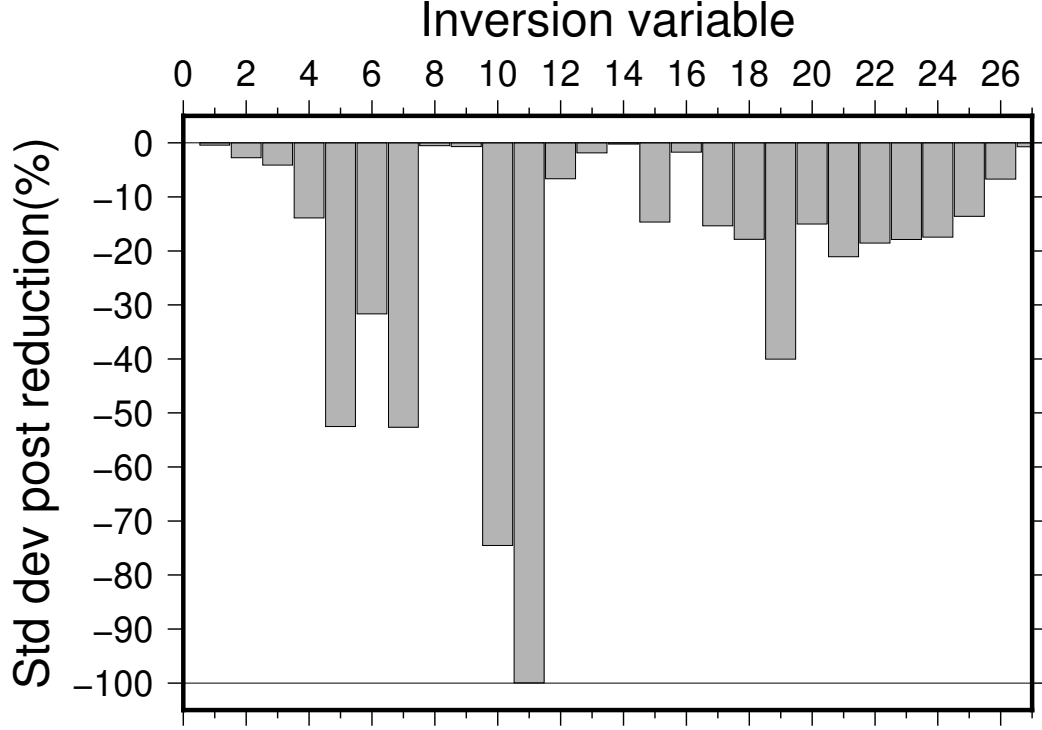The inversion presented in Section 3 is framed into a homogeneous pa-

Figure 16: Model covariance reduction (corresponding standard deviations from $\tilde{\mathbf{C}}_M$ minus those from $\mathbf{C}_M$) for the different model variables in the inversion for physical state in the WC column (Table 1). Variable 1 is the thermal lithospheric buffer thickness, 2-4 are the crustal densties, 5-7 are crustal $V_s$, 8 and 9 are the depth of the upper and lower crustal discontinuities, respectively, 10 and 11 are the Moho and LAB depths, 12-14 are the sublithospheric temperatures, 15-16 are the lithospheric and sublithospheric mantle composition, and 17-26 the are the radial anisotropy in the vertical nodes (see text for further details).
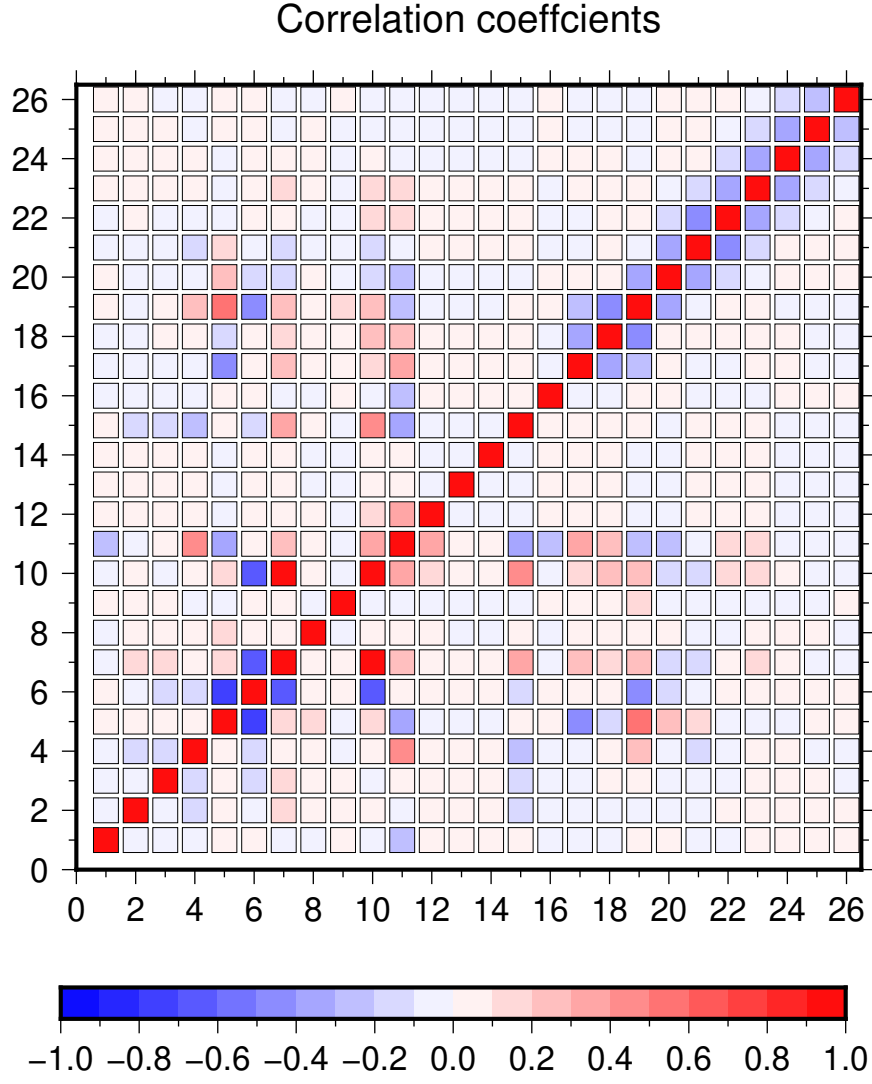
63

Figure 17: $\tilde{\mathbf{C}}_M$-derived correlation matrix (37) for in the WC column (Table 1) corresponding to the standard deviation reductions shown in Fig. 16. Variable 1 is the thermal lithospheric buffer thickness, 2-4 are the crustal densties, 5-7 are crustal $V_s$, 8 and 9 are the depth of the upper and lower crustal discontinuities, respectively, 10 and 11 are the Moho and LAB depths, 12-14 are the sublithospheric temperatures, 15-16 are the lithospheric and sublithospheric mantle composition, and 17-26 the are the radial anisotropy in the vertical nodes (see text for further details).

rameter space defined by one secondary physical parameter (i.e., electrical resistivity). The specific physical problem solved in this case is a 3-D MT data inversion where the aim is to capture the spatial variations of resistivity as realistically as currently feasible to reveal the underlying physics of induction for complicated geological structures. The case study is used to illustrate typical practical problems found in geophysical inversions: finding the appropriate balance between regularization and data fit, the effect of data coverage, and the influence of the model parameterization. The map view plots from the case study inversion (e.g., Figure 4) are useful to identify tectonic boundaries or investigate subsurface geological processes affecting the electrical resistivity of the crust and upper mantle. However, it is difficult to resolve the lithosphere-asthenosphere boundary from the vertical slices in Figure 7 or in general to uniquely translate the obtained conductivity maps into lithospheric temperature, composition, or other properties of geological interest.

In section 4 we present a second case study showing a 1-D joint inversion of seismic, topography and surface heat flow data for thermochemical structure in two representative lithospheric columns for differing physiographic provinces in the western U.S. We present a general methodology and illustrate some of the issues stemming from an inversion where the parameter space is complex and defined by both primary (e.g., temperature) and secondary (e.g., crustal seismic velocity) physical magnitudes. The heterogeneous forward problems spanning geophysics, petrology and mineral physics involved (e.g., heat equation, wave propagation, thermodynamic Gibbs free energy minimization, and anelasticity) are currently tractable for simplified

65

(e.g. 1-D profiling)model geometry or smaller models, strong (e.g., reference model) regularization compared to inversions solely based on secondary parameters. Furthermore, geophysical inversions for the Earth's physical state are highly dependent on the availability and quality, of suitable theoretical relationships and laboratory measurements connecting secondary physical parameters (e.g., seismic velocities or resistivity) with the fundamental variables generally used to describe Earth's interior (e.g., temperature, composition, melt fraction, etc.). An advantage of this type of joint inversion is it can be directly used to invert for physical state and to assess consistency between diverse forward modeling approaches, bearing in mind the aforementioned limitations. For instance, in our case study in section 4 Figure 13 can be interpreted directly in terms of lithospheric thickness and composition, or crustal temperatures by a wide range of Earth scientists outside of geophysics. As a byproduct of the inversion, additional models of secondary parameters relevant to the forward geophysical problems involved (i.e., mantle seismic velocities and density) are also produced. We note, promisingly, that these secondary parameter models are mutually consistent when linked to the common primary parameters defining the Earth's physical state in the joint integrated inversion.

As is commonly noted "All models are wrong, but some models are useful" (Box, 1976) – neither of the two case study lithospheric models presented here of course captures the complete truth of Earth's subsurface, but each provides useful information about insightful aspects. The choice of the particular geophysical inversion method and parameterization should always be directed by data availability and type, a strong knowledge of the uncertainty and

resolution issues, and overall by scientific objectives.

Considering the mechanics of the inversion and some of the major choices that must be made when performing, evaluating, and interpreting geophysical inversions, we note that these must include the degree of fit to the data (and the reliability of data error estimates), the selection and availability of instrumentation sites, and the form of the model discretization, an understanding of resolution and bias, and assessment of parameter uncertainties and correlations. A sign of robustness in the case studies presented here is that fundamental large-scale structures (in the electrical resistivity pattern and thermal thickness of the lithosphere) are consistently reproduced in multiple and independently derived models, with intriguing differences that may indicate new science or may arise from data limitations or methodological artefacts. In making progress, the details of the inversion procedure, particularly the effects of regularization and resolution, do matter and need to be carefully laid out and justified. Parameter correlation and resolution tests are essential tools in this. Unfortunately, for very large-scale models, full uncertainty and resolution analyses, either deterministic or statistical, may be intractable due to computational limitations. In the 1-D integrated inversion study case presented here the reduced size of the problem allows us to use some of the theoretical tools presented in section 2 to assess the inversion. The reduction in model covariance and the correlation between different model parameters (Figures 16 and 17 ) provide insight on the trade-off dependencies between parameters and allow us to test different modelling assumptions (e.g. thermal steady state, local isostasy, anelasticity), regularization influences, and parameterization and on inversion resolution and to

more clearly map the influences and modeling consistencies of the data.

In summary, modern geophysical inversion approaches provide a wealth of information about the structure and composition of the lithosphere provided quality data with appropriate coverage are available. As with any other scientific technique, it is crucial to understand the capabilities and limitations of geophysical inversions to avoid mis- or over-interpretation of the data, and to present these limitations openly and in an interpretable form. The last 40 years of work in computational geophysical inverse methods coupled with significant contributions from petrology and mineral physics have resulted in algorithms that produce stable and reliable results for increasingly large-scale and multi-data/multi-parameter problems. However, the more details and precision we require, the more we have to assess the impact of our inversion choices on the results. The risk of exploiting a powerful black box that will always produce an Earth model is only too tantalizing. In this paper we present an overview of useful theoretical and practical aspects regarding inversion modelling, and we point to questions that one should always ask about the output models. We hope that this will help practitioners concerned with interpreting results, and improving on, of geophysical inversions in an increasingly multidisciplinary context.

## 6. Acknowledgments

## 7. Appendix. A Simple Example of a Geophysical Problem

As a simple demonstration of the concepts described in Section 2, consider a simplified linear inverse problem of determining the density of two Bouguer gravity anomaly slabs of known thickness. The forward problem, for a single data point, $d$, is (e.g., Lowrie, 2007)

$$d = 2\pi\Gamma\left(h_1\rho_1 + h_2\rho_2\right) \tag{38}$$

where $\Gamma$ is Newton's gravitational constant, $d$ is a gravity measurement, and $\rho_1$ and $\rho_2$ are the respective slab densities

To further simplify the example, we set $h_1 = h_2 = h$, giving

$$d = 2\pi\Gamma h\left(\rho_1 + \rho_2\right). \tag{39}$$

It is obvious that: i) If we disregard noise, we will always get the same result, as the data, $d$ are independent of position. So, adding more measurements will not give us new information unless there is data noise present. ii) We cannot determine $\rho_1$ and $\rho_2$ independently, any combination of densities that has the same sum will fit the data equally well.

The generalization of the forward problem for two measurements is

$$\underbrace{\begin{bmatrix} d_1 \\ d_2 \end{bmatrix}}_{\mathbf{d}} = \underbrace{2\pi\Gamma h \begin{bmatrix} 1 & 1 \\ 1 & 1 \end{bmatrix}}_{\mathbf{G}} \underbrace{\begin{bmatrix} \rho_1 \\ \rho_2 \end{bmatrix}}_{\mathbf{m}} \tag{40}$$

$\mathbf{G}$ is square but is not invertible (it is rank deficient). The model null space can be seen by inspection to be the set of all vectors $\kappa(-1,\ 1)$, where $\kappa$ is a scalar. To produce a unique solution, it is necessary to introduce regularization. For example, if we desire that the solution be small in the sense that its Euclidian (2–norm) length

$$\|\mathbf{m}\|\|_2 = \sqrt{\rho_1^2 + \rho_2^2} \tag{41}$$

is small (first-order Tikhonov regularization), we solve a modified system of equations

$$\begin{bmatrix} d_1 \\ d_2 \\ 0 \\ 0 \end{bmatrix} = \begin{bmatrix} \mathbf{G} \\ \alpha\mathbf{I} \end{bmatrix} \begin{bmatrix} \rho_1 \\ \rho_2 \end{bmatrix} \tag{42}$$

where $\mathbf{I}$ is the 2 by 2 identity matrix and $\alpha$ is a scalar trade-off parameter. The magnitude of $\alpha$ controls the weighting of the constraint equations between achieving a least-squares fit to the data ($\alpha$ small) and minimizing the solution 2–norm ($\alpha$ large). This can be seen more explicitly in noting that the 2–norm generalized residual in (14) in this regularized system of equations (42) produces an *objective function* ("penalty" function to be minimized) of

$$\|\mathbf{d} - \mathbf{Gm}\|_2^2 + \alpha^2 \|\mathbf{m}\|_2^2 \ . \tag{43}$$

The corresponding normal equations solution for (42) is

$$\mathbf{m}_\dagger = \mathbf{G}^\dagger \mathbf{d} \tag{44}$$

where

$$\mathbf{G}^\dagger = \left(\mathbf{G}^T\mathbf{G} + \alpha^2\mathbf{I}\right)^{-1}\mathbf{G}^T . \tag{45}$$

Applying some elemental matrix algebra gives the generalized inverse matrix

$$\mathbf{G}^\dagger = \frac{1}{2\pi\Gamma h}\begin{bmatrix} \frac{1}{\alpha^2+4} & \frac{1}{\alpha^2+4} \\ \frac{1}{\alpha^2+4} & \frac{1}{\alpha^2+4} \end{bmatrix} \tag{46}$$

and the solution

$$\rho_1 = \rho_2 = \frac{1}{2\pi\Gamma h}\frac{d_1 + d_2}{\alpha^2 + 4} \tag{47}$$

which for no noise, i.e., $d_1 = d_2$, and in the limit as $\alpha = 0$, results in an unregularized and unbiased solution that fits the data exactly and has minimum model 2–norm (41). In the presence of noise this solution is proportional to the average of the two data values. This weighted averaging property of least-squares solutions generalizes to many measurements. Furthermore, if the data noise is Gaussian (described by a multivariate normal, or MVN, distribution), the model parameter estimates for an unregularized least-squares solution to any linear inverse problem will also be Gaussian, since the model parameters are all linear combinations of the data elements. However, if $\alpha = 0$, the expression (46) for $\mathbf{G}^\dagger$ is invalid, since $\mathbf{G}^T\mathbf{G}$ is singular. Introducing a value of $\alpha > 0$ creates an invertible matrix in (46), but introduces a bias that, in this case results in a reduction in the recovered densities. Although this particular problem is not ill-posed, as noted above the addition of regularization does commonly offer the additional advantage of stabilizing

ill-posed systems of equations as reflected by a reduction in the condition number (16).

The selection of an optimal balance between regularization and data fit commonly involves assessing the trade-off between data fit and model regularization. Two commonly used methods of selecting the trade-off parameter ($\alpha$, here) are the *discrepancy principle*, in which the (noisy) data are fit only to an appropriate tolerance based on understanding of the data noise levels (e.g., Farquharson and Oldenburg, 2004), and the estimation of an optimal corner in the $\alpha$-parameterized curve describing the relationship between data fit and model regularization for a range of solutions (e.g., Moorkamp et al., 2010).

Finally, we examine the resolution matrix

$$\mathbf{R} = \mathbf{G}^{\dagger}\mathbf{G} = \begin{bmatrix} \frac{2}{4+\alpha^2} & \frac{2}{4+\alpha^2} \\ \frac{2}{4+\alpha^2} & \frac{2}{4+\alpha^2} \end{bmatrix} \tag{48}$$

that describes the "smearing" of model information across the model due to limited resolution. In this case, a true model ($\rho_1$, $\rho_2$) would produce noise-free data that would then produce the inverse solution

$$\rho_1 = \rho_2 = \frac{2}{4 + \alpha^2}(\rho_1 + \rho_2) \ . \tag{49}$$

The form of (48) thus reflects that this inverse problem is wholly unable to resolve differences between the two slab densities but can resolve their average. Equivalently, any model described by a null space vector $\kappa(-1, \ 1)$ can be added to a solution without affecting data fit.

## 8. References

Afonso, J., Fullea, J., Griffin, W., Yang, Y., Jones, A., D. Connolly, J., O'Reilly, S., 2013a. 3-d multiobservable probabilistic inversion for the compositional and thermal structure of the lithosphere and upper mantle. I: a priori petrological information and geophysical observables. Journal of Geophysical Research: Solid Earth 118 (5), 2586–2617.

Afonso, J. C., Fernandez, M., Ranalli, G., Griffin, W., Connolly, J., 2008. Integrated geophysical-petrological modeling of the lithosphere and sub-lithospheric upper mantle: Methodology and applications. Geochemistry, Geophysics, Geosystems 9 (5).

Afonso, J. C., Fullea, J., Yang, Y., Connolly, J., Jones, A., 2013b. 3-d multi-observable probabilistic inversion for the compositional and thermal structure of the lithosphere and upper mantle. II: General methodology and resolution analysis. Journal of Geophysical Research: Solid Earth 118 (4), 1650–1676.

Afonso, J. C., Moorkamp, M., Fullea, J., 2016a. Imaging the lithosphere and upper mantle: Where we are at and where we are going. Integrated Imaging of the Earth: Theory and Applications, Geophysical Monograph 218, 191–218.

Afonso, J. C., Rawlinson, N., Yang, Y., Schutt, D. L., Jones, A. G., Fullea, J., Griffin, W. L., 2016b. 3-D multiobservable probabilistic inversion for the compositional and thermal structure of the lithosphere and upper mantle:

III. Thermochemical tomography in the western-central US. Journal of Geophysical Research: Solid Earth 121 (10), 7337–7370.

Aster, R., Thurber, C., Borchers, B., 2018. Parameter Estimation and Inverse Problems, Third Edition. Elsevier Academic Press.

Avdeev, D. B., 2005. Three-dimensional electromagnetic modelling and inversion from theory to application. Surveys in Geophysics 26 (6), 767–799.

Avdeeva, A., Moorkamp, M., Avdeev, D., Jegen, M., Miensopust, M., 2015. Three-dimensional inversion of magnetotelluric impedance tensor data and full distortion matrix. Geophysical Journal International 202 (1), 464–481.

Bartzsch, S., Lebedev, S., Meier, T., 2011. Resolving the lithosphere–asthenosphere boundary with seismic rayleigh waves. Geophysical Journal International 186 (3), 1152–1164.

Baumeister, J., 1987. Stable Solution of Inverse Problems. Vieweg, Braunschweig.

Bedrosian, P. A., Feucht, D. W., 2014. Structure and tectonics of the northwestern united states from earthscope usarray magnetotelluric data. Earth and Planetary Science Letters 402, 275–289.

Ben Mansour, W., England, R. W., Fishwick, S., Moorkamp, M., 2018. Crustal properties of the northern Scandinavian mountains and Fennoscandian shield from analysis of teleseismic receiver functions. Geophysical Journal International 214 (1), 386–401.

Bonadio, R., Geissler, W. H., Lebedev, S., Fullea, J., Ravenna, M., Celli, N. L., Jokat, W., Jegen, M., Sens-Schönfelder, C., Baba, K., 2018. Hot upper mantle beneath the Tristan da Cunha Hotspot from probabilistic Rayleigh-wave inversion and petrological modeling. Geochemistry, Geophysics, Geosystems 19 (5), 1412–1428.

Box, G. E. P., 1976. Science and statistics. Journal of the American Statistical Association 71 (356), 791–799.
URL https://www.tandfonline.com/doi/abs/10.1080/01621459.1976.10480949

Bozdağ, E., Peter, D., Lefebvre, M., Komatitsch, D., Tromp, J., Hill, J., Podhorszki, N., Pugmire, D., 2016. Global adjoint tomography: First-generation model. Geophysical Journal International 207 (3), 1739.

Cammarano, F., Goes, S., Vacher, P., Giardini, D., 2003. Inferring upper-mantle temperatures from seismic velocities. Physics of the Earth and Planetary Interiors 138 (3-4), 197–222.

Celli, N., 2020. Regional-scale structure and dynamics of the crust, upper mantle and transition zone from waveform tomography with massive datasets. Ph.D. Thesis.

Chantel, J., Manthilake, G., Andrault, D., Novella, D., Yu, T., Wang, Y., 2016. Experimental evidence supports mantle partial melting in the asthenosphere. Science Advances 2 (5).
URL https://advances.sciencemag.org/content/2/5/e1600246

Chave, A. D., 2017. Estimation of the magnetotelluric response function: The

path from robust estimation to a stable maximum likelihood estimator. Surveys in Geophysics 38 (5), 837–867.

Chave, A. D., Jones, A. G., 2012. The magnetotelluric method: Theory and practice. Cambridge University Press.

Connolly, J., 2009. The geodynamic equation of state: what and how. Geochemistry, Geophysics, Geosystems 10 (10).

Connolly, J., Kerrick, D., 2002. Metamorphic controls on seismic velocity of subducted oceanic crust at 100–250 km depth. Earth and Planetary Science Letters 204 (1-2), 61–74.

Connolly, J. A., 2005. Computation of phase equilibria by linear programming: a tool for geodynamic modeling and its application to subduction zone decarbonation. Earth and Planetary Science Letters 236 (1-2), 524–541.

DeNosaquo, K. R., Smith, R. B., Lowry, A. R., 2009. Density and lithospheric strength models of the yellowstone–snake river plain volcanic system from gravity and heat flow data. Journal of Volcanology and Geothermal Research 188 (1-3), 108–127.

Dong, H., Wei, W., Jin, S., Ye, G., Zhang, L., Yin, Y., Xie, C., Jones, A. G., et al., 2016. Extensional extrusion: Insights into south-eastward expansion of tibetan plateau from magnetotelluric array data. Earth and Planetary Science Letters 454, 78–85.

Durek, J. J., Ekström, G., 1996. A radial model of anelasticity consistent

with long-period surface-wave attenuation. Bulletin of the Seismological Society of America 86 (1A), 144–158.

Eaton, D. W., Darbyshire, F., Evans, R. L., Grtter, H., Jones, A. G., Yuan, X., 2009. The elusive lithosphere–asthenosphere boundary (LAB) beneath cratons. Lithos 109 (1), 1–22.
URL http://www.sciencedirect.com/science/article/pii/S0024493708001096

Egbert, G., Kelbert, A., 2012. Computational recipes for electromagnetic inverse problems. Geophysical Journal International 189 (1), 251–267.

Evans, R. L., Jones, A. G., Garcia, X., Muller, M., Hamilton, M., Evans, S., Fourie, C., Spratt, J., Webb, S., Jelsma, H., et al., 2011. Electrical lithosphere beneath the Kaapvaal craton, southern Africa. Journal of Geophysical Research: Solid Earth 116 (B4).

Farquharson, C. G., Oldenburg, D. W., 1998. Non-linear inversion using general measures of data misfit and model structure. Geophysical Journal International 134, 213–227.

Farquharson, C. G., Oldenburg, D. W., 2004. A comparison of automatic techniques for estimating the regularization parameter in non-linear inverse problems. Geophysical Journal International 156 (3), 411–425.

Faul, U. H., Jackson, I., 2005. The seismological signature of temperature and grain size variations in the upper mantle. Earth and Planetary Science Letters 234 (1-2), 119–134.

Fichtner, A., Kennett, B. L., Igel, H., Bunge, H.-P., 2009. Full seismic waveform tomography for upper-mantle structure in the australasian region

using adjoint methods. Geophysical Journal International 179 (3), 1703–1725.

Fichtner, A., Trampert, J., 2011. Resolution analysis in full waveform inversion. Geophysical Journal International 187 (3), 1604–1624.
URL http://dx.doi.org/10.1111/j.1365-246X.2011.05218.x

Fishwick, S., 2010. Surface wave tomography: Imaging of the lithosphere-asthenosphere boundary beneath central and southern Africa? Lithos 120 (1-2), 63–73.

Foster, K., Dueker, K., Schmandt, B., Yuan, H., 2014. A sharp cratonic lithosphere–asthenosphere boundary beneath the American Midwest and its relation to mantle flow. Earth and Planetary Science Letters 402, 82–89.

Fullea, J., 2017. On joint modelling of electrical conductivity and other geophysical and petrological observables to infer the structure of the lithosphere and underlying upper mantle. Surveys in Geophysics 38 (5), 963–1004.

Fullea, J., Afonso, J. C., Connolly, J., Fernandez, M., García-Castellanos, D., Zeyen, H., 2009. Litmod3d: An interactive 3-d software to model the thermal, compositional, density, seismological, and rheological structure of the lithosphere and sublithospheric upper mantle. Geochemistry, Geophysics, Geosystems 10 (8).

Fullea, J., Camacho, A. G., Negredo, A. M., Fernández, J., 2015. The Canary Islands hot spot: New insights from 3D coupled geophysical–petrological

modelling of the lithosphere and uppermost mantle. Earth and Planetary Science Letters 409, 71–88.

Fullea, J., Lebedev, S., Agius, M., Jones, A., Afonso, J. C., 2012. Lithospheric structure in the baikal–central mongolia region from integrated geophysical-petrological inversion of surface-wave data and topographic elevation. Geochemistry, Geophysics, Geosystems 13 (8).

Fullea, J., Muller, M., Jones, A., 2011. Electrical conductivity of continental lithospheric mantle from integrated geophysical and petrological modeling: Application to the Kaapvaal Craton and Rehoboth Terrane, southern Africa. Journal of Geophysical Research: Solid Earth 116 (B10).

Gaillard, F., 2004. Laboratory measurements of electrical conductivity of hydrous and dry silicic melts under pressure. Earth and Planetary Science Letters 218 (1), 215 – 228.
URL http://www.sciencedirect.com/science/article/pii/S0012821X03006393

Glover, P. W., 2010. A generalized archies law for n phases. Geophysics 75 (6), E247–E265.

Goes, S., Govers, R., Vacher, P, 2000. Shallow mantle temperatures under europe from p and s wave tomography. Journal of Geophysical Research: Solid Earth 105 (B5), 11153–11169.

Hammond, W. C., Humphreys, E. D., 2000. Upper mantle seismic wave velocity: Effects of realistic partial melt geometries. Journal of Geophysical Research: Solid Earth 105 (B5), 10975–10986.

Hansen, S. M., Dueker, K., Schmandt, B., 2015. Thermal classification of lithospheric discontinuities beneath USArray. Earth and Planetary Science Letters 431, 36–47.

Hetényi, G., Molinari, I., Clinton, J., Bokelmann, G., Bondár, I., Crawford, W. C., Dessa, J.-X., Doubre, C., Friederich, W., Fuchs, F., et al., 2018. The AlpArray seismic network: A large-scale European experiment to image the Alpine Orogen. Surveys in Geophysics 39 (5), 1009–1033.

Jackson, I., Faul, U. H., 2010. Grainsize-sensitive viscoelastic relaxation in olivine: Towards a robust laboratory-based model for seismological application. Physics of the Earth and Planetary Interiors 183 (1-2), 151–163.

Jackson, I., Fitz Gerald, J. D., Faul, U. H., Tan, B. H., 2002. Grain-size-sensitive seismic wave attenuation in polycrystalline olivine. Journal of Geophysical Research: Solid Earth 107 (B12), ECV 5–1–ECV 5–16.

Jones, A., Fishwick, S., Evans, R., Muller, M., Fullea, J., 2013. Velocity-conductivity relations for cratonic lithosphere and their application: Example of Southern Africa. Geochemistry, Geophysics, Geosystems 14 (4), 806–827.

Karato, S., 2012. On the origin of the asthenosphere. Earth and Planetary Science Letters 321, 95–103.

Karato, S., Dai, L., 2009. Comments on "Electrical conductivity of wadsleyite as a function of temperature and water content by Manthilake et al. Physics of the Earth and Planetary Interiors 174 (1), 19 – 21, advances in High Pressure Mineral Physics: from Deep Mantle to the Core.

Karato, S.-i., 1993. Importance of anelasticity in the interpretation of seismic tomography. Geophysical Research Letters 20 (15), 1623–1626.

Karato, S.-i., 2008. Deformation of Earth materials. An Introduction to the Rheology of Solid Earth 463.

Katz, R. F., Spiegelman, M., Langmuir, C. H., 2003. A new parameterization of hydrous mantle melting. Geochemistry, Geophysics, Geosystems 4 (9).

Kawakatsu, H., Kumar, P., Takei, Y., Shinohara, M., Kanazawa, T., Araki, E., Suyehiro, K., 2009. Seismic evidence for sharp lithosphere-asthenosphere boundaries of oceanic plates. Science 324 (5926), 499–502.

Kelbert, A., 2019. Taking magnetotelluric data out of the drawer. AGUFM 2019, IN21A–01.

Kelbert, A., Egbert, G. D., deGroot Hedlin, C., 2012. Crust and upper mantle electrical conductivity beneath the Yellowstone hotspot track. Geology 40 (5), 447–450.

Kennett, B. L., Engdahl, E., Buland, R., 1995. Constraints on seismic velocities in the earth from traveltimes. Geophysical Journal International 122 (1), 108–124.

Khan, A., Boschi, L., Connolly, J., 2009. On mantle chemical and thermal heterogeneities and anisotropy as mapped by inversion of global surface wave data. Journal of Geophysical Research: Solid Earth 114 (B9).

Khan, A., Boschi, L., Connolly, J. A. D., 2011. Mapping the earth's thermo-

chemical and anisotropic structure using global surface wave data. Journal of Geophysical Research: Solid Earth 116 (B1).

Khan, A., Connolly, J., Olsen, N., 2006. Constraining the composition and thermal state of the mantle beneath europe from inversion of long-period electromagnetic sounding data. Journal of Geophysical Research: Solid Earth 111 (B10).

Kind, R., Yuan, X., Kumar, P., 2012. Seismic receiver functions and the lithosphere–asthenosphere boundary. Tectonophysics 536, 25–43.

Kirsch, A., 1996. An Introduction to the Mathematical Theory of Inverse Problems. Springer–Verlag, New York.

Kolawole, F., Atekwana, E. A., Malloy, S., Stamps, D. S., Grandin, R., Abdelsalam, M. G., Leseane, K., Shemang, E. M., 2017. Aeromagnetic, gravity, and differential interferometric synthetic aperture radar analyses reveal the causative fault of the 3 April 2017 mw 6.5 Moiyabana, Botswana, earthquake. Geophysical Research Letters, n/a–n/a2017GL074620.

Kuskov, O., Kronrod, V., Prokofyev, A., Pavlenkova, N., 2014. Thermochemical structure of the lithospheric mantle underneath the Siberian craton inferred from long-range seismic profiles. Tectonophysics 615, 154–166.

Laske, G., Masters, G., Ma, Z., Pasyanos, M., 2013. Update on crust1. 0a 1-degree global model of earths crust. In: Geophys. Res. Abstr. Vol. 15. EGU General Assembly Vienna, Austria, p. 2658.

Laumonier, M., Farla, R., Frost, D. J., Katsura, T., Marquardt, K., Bouvier,

A.-S., Baumgartner, L. P., 2017. Experimental determination of melt interconnectivity and electrical conductivity in the upper mantle. Earth and Planetary Science Letters 463, 286–297.

Lebedev, S., Nolet, G., Meier, T., Van Der Hilst, R. D., 2005. Automated multimode inversion of surface and s waveforms. Geophysical Journal International 162 (3), 951–964.

Lebedev, S., Van Der Hilst, R. D., 2008. Global upper-mantle tomography with the automated multimode inversion of surface and s-wave forms. Geophysical Journal International 173 (2), 505–518.

Li, J., Dong, S., Cawood, P. A., Zhao, G., Johnston, S. T., Zhang, Y., Xin, Y., 2018. An andean-type retro-arc foreland system beneath northwest south china revealed by sinoprobe profiling. Earth and Planetary Science Letters 490, 170–179.

Liu, H.-P., Anderson, D. L., Kanamori, H., 1976. Velocity dispersion due to anelasticity; implications for seismology and mantle composition. Geophysical Journal International 47 (1), 41–58.

Lloyd, A. J., Wiens, D. A., Zhu, H., Tromp, J., Nyblade, A. A., Aster, R. C., Hansen, S. E., Dalziel, I. W. D., Wilson, T. J., Ivins, E. R., ODonnell, J. P., 2019. Seismic structure of the antarctic upper mantle based on adjoint tomography. Journal of Geophysical Research: Solid Earth.

Long, M. D., Levander, A., Shearer, P. M., 2014. An introduction to the special issue of Earth and Planetary Science Letters on USArray science.

Lowrie, W., 2007. Fundamentals of Geophysics, 2nd Edition. Cambridge University Press.

MacCarthy, J. K., Borchers, B., Aster, R., 2011. Efficient stochastic estimation of the model resolution matrix diagonal and generalized crossvalidation for large geophysical inverse problems. J. Geophys. Res. 116, B10304.

Malinverno, A., Briggs, V. A., 2004. Expanded uncertainty quantification in inverse problems: Hierarchical bayes and empirical bayes. Geophysics 69 (4), 1005–1016.

Masters, G., Woodhouse, J., Freeman, G., 2011. Mineos v1.0.2 [software], computational infrastructure for geodynamics. https://geodynamics.org/cig/software/mineos/.

Matas, J., Bass, J., Ricard, Y., Mattern, E., Bukowinski, M., 2007. On the bulk composition of the lower mantle: predictions and limitations from generalized inversion of radial seismic profiles. Geophysical Journal International 170 (2), 764–780.

Maus, S., Haak, V., 2003. Magnetic field annihilators: invisible magnetization at the magnetic equator. Geophysical Journal International 155 (2), 509–513.

Menke, W., 1989. Geophysical Data Analysis: Discrete Inverse Theory, revised Edition. Vol. 45 of International Geophysics Series. Academic Press, San Diego.

Meqbel, N. M., Egbert, G. D., Wannamaker, P. E., Kelbert, A., Schultz, A., 2014. Deep electrical resistivity structure of the northwestern US derived

from 3-D inversion of USArray magnetotelluric data. Earth and Planetary Science Letters 402, 290–304.

Miensopust, M. P., 2017. Application of 3-d electromagnetic inversion in practice: Challenges, pitfalls and solution approaches. Surveys in Geophysics 38 (5), 869–933.

Miller, K. J., Montsi, L. G., lu Zhu, W., 2015. Estimates of olivinebasaltic melt electrical conductivity using a digital rock physics approach. Earth and Planetary Science Letters 432, 332 – 341.
URL http://www.sciencedirect.com/science/article/pii/S0012821X15006329

Minster, J. B., Anderson, D. L., 1981. A model of dislocation-controlled rheology for the mantle. Philosophical Transactions of the Royal Society of London. Series A, Mathematical and Physical Sciences 299 (1449), 319–356.

Mooney, W. D., 2015. Crust and Lithospheric Structure - Global Crustal Structure. In: Schubert, G. (Ed.), Treatise on Geophysics (2nd Edition). Elsevier, Ch. 1-11, pp. 339–390.

Moorkamp, M., Fishwick, S., Walker, R. J., Jones, A. G., 2019. Geophysical evidence for crustal and mantle weak zones controlling intra-plate seismicity–the 2017 Botswana earthquake sequence. Earth and Planetary Science Letters 506, 175–183.

Moorkamp, M., Jones, A. G., Fishwick, S., 2010. Joint inversion of receiver functions, surface wave dispersion and magnetotelluric data. Journal of Geophysical Research: Solid Earth 115, B04318.

Ni, H., Keppler, H., Behrens, H., 2011. Electrical conductivity of hydrous basaltic melts: implications for partial melting in the upper mantle. Contributions to Mineralogy and Petrology 162 (3), 637–650.

Nocedal, J. und Wright, S., 2006. Numerical Optimization. Springer.

O'Donnell, J. P., Selway, K., Nyblade, A. A., Brazier, R. A., Wiens, D. A., Anandakrishnan, S., Aster, R. C., Huerta, A. D., Wilson, T., Winberry, J. P., 2017. The uppermost mantle seismic velocity and viscosity structure of central west antarctica. Earth and Planetary Science Letters 472, 38–49.

Patro, P. K., Egbert, G. D., 2008. Regional conductivity structure of Cascadia: Preliminary results from 3D inversion of USArray transportable array magnetotelluric data. Geophysical Research Letters 35 (20).

Piazzoni, A., Steinle-Neumann, G., Bunge, H.-P., Dolejš, D., 2007. A mineralogical model for density and elasticity of the Earth's mantle. Geochemistry, Geophysics, Geosystems 8 (11).

Podvin, P., Lecomte, I., 1991. Finite difference computation of traveltimes in very contrasted velocity models: A massively parallel approach and its associated tools. Geophysical Journal International 105, 271–284.

Priestley, K., McKenzie, D., 2006. The thermal structure of the lithosphere from shear wave velocities. Earth and Planetary Science Letters 244 (1-2), 285–301.

Priestley, K., McKenzie, D., 2013. The relationship between shear wave velocity, temperature, attenuation and viscosity in the shallow part of the mantle. Earth and Planetary Science Letters 381, 78–91.

Rao, C., Jones, A. G., Moorkamp, M., Weckmann, U., 2014. Implications for the lithospheric geometry of the Iapetus suture beneath Ireland based on electrical resistivity models from deep-probing magnetotellurics. Geophysical Journal International 198 (2), 737–759.

Ricard, Y., Mattern, E., Matas, J., 2005. Synthetic tomographic images of slabs from mineral physics. Earth's Deep Mantle: Structure, Composition, and Evolution 160, 283–300.

Robertson, K., Heinson, G., Thiel, S., 2016. Lithospheric reworking at the Proterozoic–Phanerozoic transition of Australia imaged using AusLAMP Magnetotelluric data. Earth and Planetary Science Letters 452, 27–35.

Romanowicz, B., 1995. A global tomographic model of shear attenuation in the upper mantle. Journal of Geophysical Research: Solid Earth 100 (B7), 12375–12394.

Roy, C., Romanowicz, B., 2017. On the implications of a priori constraints in transdimensional bayesian inversion for continental lithospheric layering. Journal of Geophysical Research: Solid Earth 122 (12), 10–118.

Rychert, C. A., Fischer, K. M., Rondenay, S., 2005. A sharp lithosphere–asthenosphere boundary imaged beneath eastern North America. Nature 436 (7050), 542–545.

Rychert, C. A., Shearer, P. M., 2009. A global view of the lithosphere-asthenosphere boundary. Science 324 (5926), 495–498.

Schaeffer, A., Lebedev, S., 2013. Global shear speed structure of the upper

mantle and transition zone. Geophysical Journal International 194 (1), 417–449.

Schmerr, N., 2012. The Gutenberg discontinuity: Melt at the lithosphere-asthenosphere boundary. Science 335 (6075), 1480–1483.

Schutt, D., Lesher, C., 2006. Effects of melt depletion on the density and seismic velocity of garnet and spinel lherzolite. Journal of Geophysical Research: Solid Earth 111 (B5).

Selby, N. D., Woodhouse, J. H., 2002. The Q structure of the upper mantle: Constraints from Rayleigh wave amplitudes. Journal of Geophysical Research: Solid Earth 107 (B5), ESE–5.

Sobolev, S. V., Zeyen, H., Stoll, G., Werling, F., Altherr, R., Fuchs, K., et al., 1996. Upper mantle temperatures from teleseismic tomography of french massif central including effects of composition, mineral reactions, anharmonicity, anelasticity and partial melt. Earth and Planetary Science Letters 139 (1), 147–164.

Stixrude, L., Lithgow-Bertelloni, C., 2005. Thermodynamics of mantle mineralsi. physical properties. Geophysical Journal International 162 (2), 610–632.

Stixrude, L., Lithgow-Bertelloni, C., 2011. Thermodynamics of mantle minerals-ii. phase equilibria. Geophysical Journal International 184 (3), 1180–1213.

Szwillus, W., Afonso, J. C., Ebbing, J., Mooney, W. D., 2019. Global crustal

thickness and velocity structure from geostatistical analysis of seismic data. Journal of Geophysical Research: Solid Earth 124 (2), 1626–1652.

Takei, Y., 2017. Effects of partial melting on seismic velocity and attenuation: A new insight from experiments. Annual Review of Earth and Planetary Sciences 45 (1), 447–470.

Tarantola, A., 1987. Inverse Problem Theory: Methods for Data Fitting and Model Parameter Estimation. Elsevier, New York.

Tarantola, A., 2005. Inverse problem theory and methods for model parameter estimation. Vol. 89. siam.

Trabant, C., Hutko, A. R., Bahavar, M., Karstens, R., Ahern, T., Aster, R., 2012. Data products at the IRIS DMC: Stepping stones for research and other applications. Seismological Research Letters 83 (5), 846–854.

Tyburczy, J. A., Waff, H. S., 1983. Electrical conductivity of molten basalt and andesite to 25 kilobars pressure: Geophysical significance and implications for charge transport and melt structure. Journal of Geophysical Research: Solid Earth 88 (B3), 2413–2430.
URL https://agupubs.onlinelibrary.wiley.com/doi/abs/10.1029/JB088iB03p02413

Vozar, J., Jones, A. G., Fullea, J., Agius, M. R., Lebedev, S., Le Pape, F., Wei, W., 2014. Integrated geophysical-petrological modeling of lithosphere-asthenosphere boundary in central Tibet using electromagnetic and seismic data. Geochemistry, Geophysics, Geosystems 15 (10), 3965–3988.

Waff, H. S., 1974. Theoretical considerations of electrical conductivity in a

partially molten mantle and implications for geothermometry. Journal of Geophysical Research 79 (26), 4003–4010.

Xu, W., Lithgow-Bertelloni, C., Stixrude, L., Ritsema, J., 2008. The effect of bulk composition and temperature on mantle seismic structure. Earth and Planetary Science Letters 275 (1-2), 70–79.

Yamauchi, H., Takei, Y., 2016. Polycrystal anelasticity at near-solidus temperatures. Journal of Geophysical Research: Solid Earth 121 (11), 7790–7820.
URL https://agupubs.onlinelibrary.wiley.com/doi/abs/10.1002/2016JB013316

Yoshino, T., 2010. Laboratory electrical conductivity measurement of mantle minerals. Surveys in Geophysics 31 (2), 163–206.

Yuan, H., Dueker, K., Stachnik, J., 2010. Crustal structure and thickness along the yellowstone hot spot track: Evidence for lower crustal outflow from beneath the eastern snake river plain. Geochemistry, Geophysics, Geosystems 11 (3).

Zhdanov, M. S., Smith, R. B., Gribenko, A., Cuma, M., Green, M., 2011. Three-dimensional inversion of large-scale earthscope magnetotelluric data based on the integral equation method: Geoelectrical imaging of the yellowstone conductive mantle plume. Geophysical Research Letters 38 (8).